Pressure-dependent regulation of Ca^{2+} signaling in the vascular endothelium

[*]Calum Wilson[1], [*]Christopher D. Saunter[2], John M. Girkin[2] & John G. McCarron[1]

[1]Strathclyde Institute of Pharmacy and Biomedical Sciences, University of Strathclyde, SIPBS Building, 161 Cathedral Street, Glasgow G4 0RE, UK. [2]Centre for Advanced Instrumentation, Biophysical Sciences Institute, Department of Physics, Durham University, South Road, Durham, DH1 3LE, UK.

Correspondence to j.m.girkin@durham.ac.uk 44 191 334 3589 or john.mccarron@strath.ac.uk 44 141 548 4119.

Running Title Pressure-dependent Ca^{2+} responses in the endothelium

Key words endothelium, Ca^{2+} signaling, imaging

[*]Contributed equally

Key points summary

- Increased pressure suppresses endothelial control of vascular tone but it remains uncertain (1) how pressure is sensed by the endothelium and (2) how the vascular response is inhibited.
- This study used a novel imaging method to study large numbers of endothelial cells in arteries which were in a physiological configuration and held and normal blood pressures.
- Increased pressure suppressed endothelial IP_3-mediated Ca^{2+} signals
- Pressure modulated endothelial cell shape.
- The changes in cell shape may alter endothelial Ca^{2+} signals by modulating the diffusive environment for Ca^{2+} near IP_3 receptors.
- Endothelial pressure-dependent mechanosensing may occur without a requirement for a conventional molecular mechanoreceptor.

Abstract

The endothelium is an interconnected network upon which hemodynamic mechanical forces act to control vascular tone and remodeling in disease. Ca^{2+} signaling is central to the endothelium's mechanotransduction and networked activity. However, challenges in imaging Ca^{2+} in large numbers of endothelial cells under conditions that preserve the intact physical configuration of pressurized arteries have limited progress in understanding how pressure-dependent mechanical forces alter networked Ca^{2+} signaling. We developed a miniature wide-field, gradient-index (GRIN) optical probe designed to fit inside an intact pressurized artery which permitted Ca^{2+} signals to be imaged with subcellular resolution in a large number (~200) of naturally-connected endothelial cells at various pressures. Chemical (acetylcholine) activation triggered spatiotemporally-complex, propagating IP_3-mediated Ca^{2+} waves that originated in clusters of cells and progressed from there across the endothelium. Mechanical stimulation of the artery, by increased intraluminal pressure, flattened the endothelial cells and suppressed IP_3-mediated Ca^{2+} signals in all activated cells. By computationally modeling Ca^{2+} release, endothelial shape changes were shown to alter the geometry of the Ca^{2+} diffusive environment near IP_3 receptor microdomains to limit IP_3-mediated Ca^{2+} signals as pressure increased. Changes in cell shape produce a geometric, microdomain-regulation of IP_3-mediated Ca^{2+} signaling to explain macroscopic pressure-dependent, endothelial-mechanosensing without the need for a conventional mechanoreceptor. The suppression of IP_3-mediated Ca^{2+} signaling may explain the decrease in endothelial activity as pressure increases. GRIN imaging provides a convenient method that provides access to hundreds of endothelial cells in intact arteries in physiological configuration.

Abbreviations

GRIN

gradient index lens

$[Ca^{2+}]_c$

cytosolic Ca^{2+} concentration

IP_3

inositol trisphosphate

IP_3R

inositol trisphosphate receptor

RyR

ryanodine receptor

TRP

transient receptor potential

Introduction

The vascular endothelium is a one cell thick layer that directs the formation of new blood vessel (angiogenesis), prevents blood clotting, regulates vascular permeability, controls arterial tone and determines the extent of smooth muscle proliferation. The endothelium's control of each of these functions arises from the cells acting as a sensitive signal processing center that detects and interprets multiple simultaneous messages such as those derived from mechanical stimuli (hydrostatic pressure, luminal shear-stress, circumferential strain) and local and blood borne signals (autocrine, paracrine, electrical signals and neurotransmitters). Endothelial stimuli are transduced to changes in the endothelial Ca^{2+} concentration to coordinate the endothelium's control of vascular activity (Behringer & Segal, 2012; Sonkusare *et al.*, 2012; Billaud *et al.*, 2014). Ca^{2+} regulates the synthesis and release of various vasoactive agents such as nitric oxide, prostacyclin, and endothelium-derived hyperpolarizing factor. Through these Ca^{2+} -dependent mediators the endothelium's control of vascular contraction, permeability, cell proliferation and angiogenesis is achieved. Therefore, central to an understanding of endothelial signal processing is an appreciation of the control of Ca^{2+}.

Two main sources of endothelial Ca^{2+} are recognized, the extracellular fluid and the intracellular stores of the endoplasmic reticulum (Moccia *et al.*, 2012). Ca^{2+} entry from the extracellular fluid may occur via a large number of ion channels on the outside (plasma) membrane. The other main cytoplasmic Ca^{2+} concentration ($[Ca^{2+}]_c$) source is the internal endoplasmic reticulum store from which release proceeds mainly via the inositol 1,4,5-trisphosphate (IP_3) receptor (IP_3R). While Ca^{2+} release via IP_3R is well established the contribution of the ryanodine receptor (RyR) to the control of endothelial Ca^{2+} (if any) is less clear (Socha *et al.*, 2012a). The sources of Ca^{2+} are not independent, Ca^{2+} influx regulates Ca^{2+} release and Ca^{2+} release regulates Ca^{2+} influx. For example, Ca^{2+} release from the endoplasmic reticulum may alter the activity of ion channels present on the plasma membrane to regulate Ca^{2+} entry either via Ca^{2+}-gated ion channels (Strotmann *et al.*, 2003) or via membrane potential changes altering passive fluxes of the ion (Behringer & Segal, 2015). Alternatively Ca^{2+} influx may alter endoplasmic reticulum Ca^{2+} content or activity of IP_3R in a Ca^{2+} -induced Ca^{2+} release like process (Earley & Brayden, 2015). Thus the local change in $[Ca^{2+}]_c$ arising from the activity of channels in the plasma

membrane or endoplasmic reticulum itself regulates the activity of ion channels to provide a feedback control of Ca^{2+} signal and modulate vascular function.

The response to mechanical stimuli involves changes in $[Ca^{2+}]_c$ and must be integrated with signals from other sensors to converge on a physiological response. Two major mechanical stimuli are shear-stress and pressure (Falcone *et al.*, 1993; Huang *et al.*, 1998; Popp *et al.*, 1998; Muller *et al.*, 1999; Marchenko & Sage, 2000; Paniagua *et al.*, 2000; Sun *et al.*, 2001; Duza & Sarelius, 2004). The endothelial response to shear-stress is well characterized and several types of activity may occur. Vascular smooth muscle relaxation may be evoked, cell migration induced and endothelial gene expression changed (Falcone *et al.*, 1993; Muller *et al.*, 1999; Shiu *et al.*, 2004; Chien, 2007). The increases in endothelial Ca^{2+} changes underlying these responses may involve several types of mechanically-sensitive ion channels forces such as Piezo1 (Li *et al.*, 2014; Ranade *et al.*, 2014), ENaC (Kusche-Vihrog *et al.*, 2014), ATP-gated P2X4 (Yamamoto *et al.*, 2006), TREK-1 (Dedman *et al.*, 2009) and various members of the TRP grouping of channels (Corey *et al.*, 2004; Maroto *et al.*, 2005; Spassova *et al.*, 2006; Janssen *et al.*, 2011). Alternatively, shear-stress-evoked activation of ion channels may be indirect and force sensed by the cytoskeleton, apical glycocalyx, mechanosensitive or membrane curvature-sensitive protein complexes or G-protein coupled receptors (Knudsen & Frangos, 1997; Thi *et al.*, 2004; Tzima *et al.*, 2005; Zimmerberg & Kozlov, 2006; Mederos y Schnitzler *et al.*, 2008; Zhao *et al.*, 2011) . The diversity of responses highlights the complexity of the response to shear-stress.

The response of the endothelium to pressure differs significantly from that of shear-stress. Rather than being activated, a *decrease* in activity may occur as mechanical stimulation (pressure) is increased (Hishikawa *et al.*, 1992; Gunduz *et al.*, 2008). The decrease in endothelial activity may suppress smooth muscle relaxation (De Bruyn *et al.*, 1994; Huang *et al.*, 1998; Paniagua *et al.*, 2000; Zhao *et al.*, 2015). In healthy human volunteers, short-term increases in arterial blood pressure cause long-lasting inhibition of endothelium-dependent dilatation (Jurva *et al.*, 2006; Phillips *et al.*, 2011). In isolated arteries, acute exposure to increases in transmural pressure may impair endothelium-dependent relaxation (Hishikawa *et al.*, 1992; Huang *et al.*, 1998; Paniagua *et al.*, 2000; Zhao *et al.*, 2015). Relatively little is known on how pressure is sensed by the endothelium, specifically when the arteries are in their natural “tubular” configuration.

The biological response of arteries to pressure depends critically on the complex, cylindrical, three-dimensional arrangement of cells and on the interactions with other cell types and may change with artery configuration. For example, in many intact arteries in their cylindrical configuration myogenic contraction occurs when the artery is subjected to circumferential stretch by increases in pressure. However, this contraction does not occur in arteries stretched, with equivalent forces, on wires (Dunn *et al.*, 1994). Increased mechanical stimulation by stretch, hypotonic cell swelling or shear stress activates TRPV4 channels (Strotmann *et al.*, 2000; Alessandri-Haber *et al.*, 2003; Loukin *et al.*, 2010), a mechanism which may contribute to flow-induced dilation (Kohler *et al.*, 2006; Mendoza *et al.*, 2010; Bubolz *et al.*, 2012). However, TRPV4 channels are also deactivated by increased stretch when transmural pressure difference is increased in pressurized arteries (Bagher *et al.*, 2012) in a cylindrical configuration. The cell shape and operative mechanical forces in a pressurized artery are quite different from experiments on isolated or cultured cells.

The carotid artery contributes to the control of cerebrovascular blood flow and cerebral vascular resistance (Mchedlishvili 1986; Faraci & Heistad, 1990). The endothelium regulates carotid artery tone. Vascular relaxation is evoked by several endothelial activators including flow (shear-stress), adrenonedullin and acetylcholine (Faraci *et al.*, 1994; Chataigneau *et al.*, 1998a; Chataigneau *et al.*, 1998b; Plane *et al.*, 1998; Ohashi *et al.*, 2005) and the endothelium may also attenuate the vascular contractile response to vasoconstrictors (Lamping & Faraci, 2001). Many of the most serious forms of cardiovascular diseases (e.g. atherosclerosis) reside in larger arteries like the carotid artery and begin with endothelial dysfunction (Deanfield *et al.*, 2007). However, studying the effects of mechanical forces like pressure on endothelial function (and dysfunction) in larger arteries in a physiological configuration has been exceptionally difficult. Assessment of endothelial function in large arteries has been largely indirect. The majority of papers in the past decade involved only the measurement of endothelium-dependent dilatation (e.g. Craig & Martin, 2012).

To study the function of endothelial cells in intact arteries, some investigations have used either wide-field or point-scanning fluorescence microscopes to visualize the endothelium through the wall of the artery (Bagher *et al.*, 2012; Sonkusare *et al.*, 2012; Tran *et al.*, 2012). However, movement of the artery in pressure myograph systems is almost unavoidable and results in the

vessel moving in and out of the focal plane, changing light levels and altering image quality to present a significant challenge to data analysis. Light scattering by the artery wall also reduces contrast and the curvature of the artery limits the number of cells that may be visualized within a single optical plane. To overcome each of these difficulties and allow the endothelium to be studied in intact arteries we have developed a miniature optical probe to record Ca^{2+} signaling from *inside* pressurized arteries. The probe has a field-of-view of 0.5 mm diameter, which allowed a large number (~200) of naturally connected endothelial cells to be imaged with subcellular resolution and has a high depth of field (141 μm) sufficient to maintain good focus across the highly curved, intact endothelial layer of a large artery. To handle the data from such a large number of cells a largely automated image processing routine was also developed. We show in native endothelial cells in their physiological configuration, that acetylcholine-evoked Ca^{2+} rises originate as IP_3-mediated Ca^{2+} signals in particular regions of the endothelium from which they progress to other cells as Ca^{2+} waves. Detection of pressure-dependent mechanical forces by the endothelium is integrated effortlessly into the same signaling pathway by geometric modulation of IP_3-evoked Ca^{2+} release brought about by changes in endothelial cell shape. We suggest the suppression of IP_3-mediated Ca^{2+} signals may underlie the inhibition of endothelial responses with increased pressure and, significantly, may not require a conventional mechanosensor for mechanotransduction to occur.

Methods

Micro-endoscope GRIN imaging probe

The GRIN microprobe was developed to fit inside pressurized arteries (Fig 1A) and consisted of a 0.5 mm diameter, 30.2 mm long, single pitch GRIN relay lens (SRL-050; Nippon Sheet Glass, USA) with a 0.5 mm x 0.5 mm x 0.5 mm aluminum coated micro-prism (66-771; Edmund Optics, USA) attached to the distal surface with ultraviolet curing optical epoxy (NAO 68; Norland Products, USA). The lens was sheathed in a surgical stainless steel tube (0.71 mm outer diameter) for mechanical protection. In this single lens configuration, the GRIN rod acts to reconjugate the image plane of detection optics through the length of the cylinder (Fig 1D). By focusing to a sufficient depth inside the GRIN rod a conventional microscope objective, the image plane can be extended beyond the front surface of the prism and into tissue (Fig 1C-E). This property renders the probe suitable for the replacement of a cannula in a custom-made pressure myograph, where the vessel must be tied to the probe to maintain pressure (Fig 1B). The focal plane of the optical system can be varied in response to diameter variations in the vessel (Fig 1C), without moving the probe, by focusing the microscope objective (Fig 1B) further into the GRIN lens (see also Flusberg *et al.*, 2008; Kim *et al.*, 2010).

A 0.1 NA GRIN probe was used to ensure a good depth of focus (141 μm) across the entire endothelial surface of curved artery. However, the use of a low NA GRIN relay lens imposes two opposing constraints on the transmission of light through the system. First, to maximize the delivery of excitation light through the GRIN rod, the NA of the excitation light should not be greater than the NA of the GRIN lens (Fig 1D). Second, to maximize fluorescence detection, the NA of the collection lens should be higher than that of the GRIN rod. The solution to these opposing constraints is to illuminate the proximal end of the GRIN lens with collimated light, which is re-collimated at the output (Fig 1E)(Saunter *et al.*, 2012) evenly illuminating the entire field of view whilst keeping the illumination constant despite probe refocusing.

The assembled GRIN probe was held in place in a custom-designed arteriograph (Fig 1G) that was mounted on the microscope stage of a standard inverted microscope (Fig 1H). The fluorescence excitation and delivery system was constructed using 30mm cage system components (Thorlabs, UK), was also mounted onto the microscope stage via a 3-axis translation

stage. Two axes of the translation stage permitted the external optical system to be coupled to the GRIN microprobe, whilst the third enabled the focus of the system to be altered. Mounting both the arteriograph and the external optical system on the stage ensured that movement of the microscope stage did not decouple the probe from the system. Fluorescence excitation was provided by a fiber-coupled diode-pumped solid-state laser operating at 488 nm, which was collimated (Fig 1B,H) before being focused by another lens and guided to the back of a 20X 0.5NA infinity-corrected microscope objective (Plan Fluor; Nikon, UK) via a dichroic mirror. Optical excitation power density, measured at the output of the GRIN probe was 1 nW μm^2. The microscope objective and a 65 mm focal length tube lens imaged fluorescence emission, returning through the probe, through an emission filter and onto a sCMOS camera (Zyla 3-Tap; Andor, UK) controlled by μManager (Edelstein *et al.*, 2010), providing an effective pixel size of 1 μm at the object plane and permitting up to 200 endothelial cells to be imaged with subcellular resolution (see *Optical Characterization*).

Optical Characterization

To demonstrate the fluorescence signal detected by the microendoscope camera, we recorded images of a diffuse fluorescein solution (1 μM; Figure 2A), and of large 15.45 ± 0.04 μm (mean ± standard deviation; dimensions provided by manufacturer) diameter fluorescent beads (FS07F; Bang Laboratories Inc, USA; Figure 2B). To image fluorescein fluorescence, the bath chamber was filled with the fluorescent solution. Large-diameter fluorescent beads were diluted in water (100x dilution in water) and left to settle on the microprobe prism surface. Figure 2A shows the normalized intensity across the center of the circular field-of-view (raw image of fluorescein fluorescence inset). Due to vignetting of the illumination light and of the fluorescence excitation by the cylindrically shaped GRIN lens, the efficiency drops to 50% at a distance approximately 150 μm from the center of the probe. Translating the focal plane 500 μm along the z-axis, beyond the distal prism surface resulted in a slight increase in fluorescence signal, relative to maxima. Note that due to the curvature of pressurized arteries, this intensity profile does not necessarily reflect that obtained in imaging experiments performed in intact arteries. Average optical excitation power density (1 nW μm^{-2}) was calculated across the full 500 μm field-of-view from power measurements made at the output of the GRIN microprobe using a photodiode power sensor and power meter (200 – 1100 nm; S120VC and PM100A; Thorlabs, UK).

To study the resolving power of the micro-endoscope, we imaged subresolution 1 μm fluorescent microspheres (F-8823; Invitrogen, UK). The mean fluorescent microsphere diameter (as provided by the manufacturer) was 1.1 μm with a coefficient of variation (standard deviation/mean) of 4%. A small droplet of a fluorescent microsphere suspension (1×10^6 dilution in water) was manually pipetted onto the distal prism surface. Fluorescent beads were left to settle on the distal prism surface before being brought into focus and imaged (Figure 2C). Line intensity profiles of the fluorescence emitted from individual beads were taken (Fig 2D). Gaussian fits of these line intensity profiles yielded a lateral resolution of 4.51 ± 0.04 μm (n = 6 beads). This measured value may be considered to be the actual resolution of our system because it is much larger than the actual size of the beads (Kim *et al.*, 2010). All optical characterization experiments were performed using the same set-up and external optics as that used for intraluminal imaging of the endothelium.

Animals and Tissue Preparation

Common carotid arteries were obtained from male Sprague-Dawley rats (250-350 *g*) killed by overdose of pentobarbital sodium (Schedule 1 procedure; Animal (Scientific Procedures) Act 1986, UK). Arteries were then cleaned of connective tissue under a dissection microscope, and visually checked for the presence of side branches. Subsequently, arteries without side branches were mounted onto two blunted and deburred 22-gauge cannula in a custom-designed imaging bath with flow provided by a peristaltic pump (PS-200, Living Systems, USA) using two lengths of suture thread. Blood was removed from the arteries by flushing the lumen with PSS for 10 minutes (150 μl/min) before the arteries were pressurized to 60 mmHg, gently heated to 37^{o}C and allowed to equilibrate at 37 ^{o}C for 30 minutes. The endothelium of mounted arteries were then selectively loaded with a fluorescent Ca^{2+} indicator by intraluminal perfusion of PSS containing the membrane permeant form of Oregon Green BAPTA-1 (20 μM, OGB-1/AM) and 0.04% Pluronic acid. Flow was stopped for 30 minutes to permit sufficient loading. Arteries were continuously superfused with PSS during this time. Following removal of excess dye, the distal cannula was removed from the artery and the artery was mounted on a GRIN microprobe and secured with suture thread. Transmural pressure was then incrementally increased to 160 mmHg, whilst stretching the artery to remove any buckle. Following this procedure, the pressure was decreased to 60 mmHg and the artery left for a further 30 minutes to equilibrate. During

equilibration arteries were tested for leaks (which may indicate side branches, tears in the vessel wall or insufficiently of sutures) by switching off the feedback on the pressure servo. Arteries that showed signs of leakage, identified as a reduction in pressure whilst closed off from the servo system, which could not be stopped by retying the sutures, were discarded.

Ca^{2+} Imaging

Endothelial Ca^{2+} signals were recorded (5 Hz) from ~200 endothelial cells in each artery by GRIN microendoscopy. The plane of focus of the GRIN imaging system was set to the endothelial layer. Arteries at resting diameter were stimulated by application of ACh (100 μM), delivered by a handheld pipette to the outside of the pressurized artery to confirm endothelial viability. Preliminary experiments established that ~80% of the cells in the field of view responded to ACh (100 μM). Arteries in which the majority of endothelial cells did not exhibit a Ca^{2+} response to ACh were discarded. To examine the effect of increases in transmural pressure, endothelial Ca^{2+} signaling was recorded at pressures within the physiological range for the artery (60 mmHg, 110 mmHg and 160 mmHg). Following each change in pressure, the imaging system was refocused on the endothelium and arteries were left to equilibrate for 20 minutes. The Ca^{2+} responses evoked by ACh at various transmural pressures were studied in single experiments and expressed relative to the control response (60 mmHg). There was significant overlap in the cells imaged at each pressure however matching individual cells was not possible. In other experiments, the extraluminal PSS was exchanged for PSS containing various pharmacological inhibitors or Ca^{2+}-free PSS and left for 20 mins, before activation again with 100 μM extraluminally-applied ACh. The Ca^{2+} responses evoked by ACh in arteries treated with pharmacological inhibitors or Ca^{2+}-free bath solution were studied (control and treatment) in the same artery and expressed relative to the control response. Following each acquisition period, the bath solution was immediately exchanged and the arteries were left for at least 20 minutes to re-equilibrate. Smooth muscle cells were not loaded with OGB-1/AM in any of our preparations, as indicated by an absence of fluorescence staining orthogonal to the longitudinal vessel axis.

Signal Analysis

Individual endothelial cells were segmented using a custom, semi-automated image processing procedure. Previous successful fully-automated image processing of endothelial Ca^{2+} signals has been achieved by assigning regions of interest (ROIs), of predetermined size and shape to image

sequences based on subcellular activity (Francis *et al.*, 2012). Here, cellular activity was used to determine the region of interest shape from the behavior of the entire cells themselves. In detail, a series of images were created to illustrate the active wavefronts by generating the forward differences of the cytoplasmic Ca^{2+} concentration ($[Ca^{2+}]_c$) change. First, to facilitate visual inspection of endothelial Ca^{2+} signals, the active Ca^{2+} wavefronts themselves were examined by generating the forward difference of $[Ca^{2+}]_c$ changes (F_t-F_{t-1}, obtained by sequential subtraction; SS; (McCarron *et al.*, 2010)). Then single images, illustrating all endothelial cells exhibiting ACh-evoked Ca^{2+} activity, were created by taking projections of the standard deviation (STDev) of intensity of SS image stacks. Unsharp masking of standard deviation projections was used to create sharpened, background-corrected STDev images, where ROIs encompassing individual cells could be easily obtained by intensity thresholding. ROIs corresponding to individual cell outlines were verified for each image series and erroneous ROIs were corrected manually. Cell outlines were stored as polygon descriptions within text (.txt) files for subsequent processing and analysis. Except for the creation of standard deviation projections (performed in FIJI; Schindelin *et al.*, 2012) and for manually splitting joined cells, all processing was performed using batch-processing algorithms in ImagePro Plus.

Individual fluorescence signals were extracted for each polygonal region from the raw image stacks using a custom program in the Python language. Fluorescence signals are expressed as baseline corrected values (F/F_0), calculated by dividing the raw signals by the average value of using a user-defined period (typically 50 frames) preceding ACh-evoked Ca^{2+} activity. There was a significant variation in the time taken for each cell to respond to ACh. To aid analysis, individual F/F_0 traces were aligned with respect to their peak rate-of-change. The alignment provides a clear illustration of total Ca^{2+} activity. Baseline values of F/F_0, peak amplitudes and the time of peak rate-of-change for each signal were calculated automatically and stored as data tables within .csv files. These .csv files were then imported into Origin 9.1 for calculation of peak changes in fluorescence intensity ($\Delta F/F_0$), and for plotting using custom analysis scripts. For presentation, an 11 point (1.2 s), 3rd order polynomial Savitzky-Golay filter was applied within Origin; all measurements were from unsmoothed traces.

Measurement of Arterial Diameter

At the end of some experiments, we recorded the diameter of arteries as pressure was increased, in 5 mmHg increments, from 0 mmHg to 200 mmHg. For videomicroscopy-based diameter measurements, arteries were illuminated with bright field illumination, which was guided to a CCD camera mounted (Sony XC-77; Sony, Japan) mounted on the side-port of the inverted microscope on which our GRIN imaging system was mounted. Images were captured from the CCD camera using Micromanager software (Edelstein *et al.*, 2010), and a USB video capture device (Dazzle; Pinnacle Systems, USA) and stored on a computer for subsequent analysis. Due to light scattering by the artery wall, the luminal diameter could not be assessed. Thus, outer artery diameter was measured using the Vessel Diameter plugin for ImageJ (Fischer *et al.*, 2010).

Histological Analysis

Rat carotid arteries were fixed at pressure after length-adjustment (to remove buckle) at 160 mmHg. Following length adjustment, lumenal PSS was replaced with Zenker's fixative. Once the lumen was filled with fixative, the artery was sealed and the pressure was immediately raised to 60 mmHg or 160 mmHg, and the extraluminal PSS was replaced with Zenker's solution. Arteries were left to fix for at least two hours – a time determined, in preliminarily experiments to be required to prevent a reduction in arterial dimensions upon removal of pressure. Following fixation, arteries were removed from the myography chamber, washed overnight in tap water and stored in 70% ethanol at 4oC until use. Arteries were paired for analysis (i.e. two arteries from each animal were fixed at the two different pressures (60 mmHg and 160 mmHg).

Following fixation, arteries were dehydrated in alcohol series (70% ethanol, 4 hours, 4 changes; 95% ethanol, 2 hours, 2 changes; 100% ethanol, 2 hours, 4 changes), cleared (1:1 mixture of 100% ethanol, 1 hour; Histoclear, overnight, 4 changes), infiltrated and embedded (Paraffin Wax, 4 hours). Wax blocks were cut into 5 μm thick sections and mounted onto slides. Slides were rehydrated in Histoclear (10 minutes, 1 change), then alcohol series (100% ethanol, 10 minutes, 1 change; 95% ethanol, 2 minutes; 70% ethanol, 2 minutes), before being washed in distilled water. Rehydrated slides were stained with Harris Hematoxylin solution (10 minutes), washed with warm running tap water (10 minutes) then Scotts tap water (1 minute), differentiated in acid alcohol (0.3%, 5 seconds), stained with Eosin (5 minutes), washed with

warm running tap water (10 minutes), then dehydrated in alcohol series (70% ethanol, 2 minutes; 95% ethanol, 2 minutes; 100% ethanol, 10 minutes, 1 change), cleared in Histoclear (10 minutes, 1 change), before being mounted with Histoclear. Stained artery cross-sections were imaged using a Leica DM LB2 microscope with a Leica DFC320 camera (Leica Microsystems, UK). The thickness of endothelial cell nuclei, used as an indication of height of the endothelial cell layer, were measured using Image Pro Plus.

Solutions and Drugs

PSS consisted of (mM): NaCl (145), KCl (4.7), 3-[N-morpholino]propane-sulphonic acid (MOPS, 2.0), NaH_2PO_4 (1.2) glucose (5.0), ethylenediamine-tetraacetic acid (EDTA, 0.02), sodium pyruvate (2.0) $MgCl_2$ (1.17), $CaCl_2$ (2.0), (pH adjusted to 7.4 with NaOH). In Ca^{2+} free PSS, no Ca^{2+} was added, the concentration of $MgCl_2$ was increased to 3.17 mM, and ethylene glycol tetraacetic acid (EGTA, 1 mM) was included.

Although a relatively high extraluminal concentration of ACh was required to activate the majority of endothelial cells, it is likely that the endothelium was not exposed to this concentration due to presence of an adventitial barrier to diffusion. The concentration of ACh in the lumen in the present experiments was estimated to be ~100 fold less than the bath concentration at the time of Ca^{2+} measurement. Two experiments support this conclusion. First in arteries surgically opened ACh (1 μM) produced approximately equivalent responses (i.e. ~80% cells responding) to ACh (100 μM) applied to the bath in intact artery. The concentration of ACh was also estimated from the time course of diffusion of fluorescein across the vascular wall in the same experimental conditions as the pressurized artery. The fractional fluorescence change (relative to the final steady-state value) at the time (10 s after addition) that ACh evoked Ca^{2+} responses was used to estimate the fraction of the ACh was present in the lumen (~1 μM). In other studies, the potency of extraluminally applied ACh was reported to be ~1/50 of intraluminally applied ACh in the dog mesenteric artery (Toda *et al.*, 1990) and 50-100 times less potent in femoral artery (Angus *et al.*, 1983; Toda *et al.*, 1988). Additionally bradykinin is unable to evoke relaxant responses in isolated porcine coronary arteries when applied extraluminally, independent of enzymatic degradation and luminal pressure, but is able to evoke responses when applied intraluminally (Tanko *et al.*, 1999).

Drugs were all obtained from Sigma except for OGB-1/AM and Pluronic F-127, which were obtained from Invitrogen. All drugs were dissolved in DMSO and diluted to working concentration in PSS such that the total volume of DMSO was less than or equal to 0.1%.

Harris Haematoxylin, Scotts tap water and Eosin were obtained from and Sigma (UK). Zenker's fixative was obtained from Fisher Scientific.

Statistics

Summarized data are expressed as means ± standard errors of the mean (SEMs). One-way ANOVA (with Tukey's post-hoc test as appropriate) was used for comparisons between groups. A p-value less that 0.05 was considered significant and n = number of animals.

Model Description

To understand how changes in cell geometry alter IP_3-evoked Ca^{2+} release, local [Ca^{2+}] in the IP_3 receptor (IP_3R) microdomain was determined computationally in the time period encompassing ion channel opening. The cytosolic concentrations of ionic Ca^{2+}, buffer and buffered Ca^{2+} are represented by $C_{Ca,cyt}$, $C_{B,cyt}$ and $C_{CaB,cyt}$ respectively. The partial differential equation governing the concentration, C_s, of a species, s, is given by:

$$\frac{\partial C_s}{\partial t} = D_s \nabla^2 C_s + \phi_s + J_s$$

Equation 1

where C_s is the concentration, D_s is the diffusion coefficient, ϕ_s is the source term derived from chemical reactions and J_s is the source term resulting from trans-membrane flux, which was taken as zero for all species except Ca^{2+}, for which it comprises IP_3R-mediated Ca^{2+} currents.

Buffering

We employed the first order mass action reaction kinetic

$$\phi_{Ca,cyt} = -K_{on}.C_{Ca,cyt}C_{B,cyt} + K_{off}C_{CaB,cyt}$$

Equation 2

$$\phi_{B,cyt} = \phi_{CaB,cyt} = -\phi_{Ca,cyt}$$

Equation 3

where K_{on} and K_{off} are the rate constants for the buffer.

Trans-membrane flux

Ca^{2+} pumps (SERCAs) and membrane (plasma and ER) leakage currents are typically continuous, low magnitude processes that function to maintain specific concentrations of Ca^{2+} in the cytosol (typically <100 nM) and the ER (typically >0.5 mM) in the long term (Table 1). This is in contrast to IP_3Rs, which are reported to open for durations of between 2 ms and 20 ms, with a transient current that is far higher than those of the aforementioned long-term processes. We therefore omitted the slow acting sources and sinks, as their effects over the brief temporal and spatial scales of an individual microdomain, with which we are concerned, are limited. The transport of Ca^{2+} from the ER to the cytosol, through an open IP_3R, is a purely diffusive process, and is therefore driven in linear proportion to the ionic concentration gradient between the two partitions. Therefore individual IP_3R are represented by the source term:

$$J_s = \alpha J_0 \frac{C_{Ca,er} - C_{Ca,cyt}}{C_{Ca,er}}$$

Equation 4

where $C_{Ca,er}$ is the concentration of Ca^{2+} in the ER, taken as a constant, J_0 is the experimentally measured maximal ion current of an isolated IP_3R and α is a conversion factor from a current (in moles per second) to a molar concentration for the voxel to which the current is applied.

Computation

Equation 1 was solved for a regular voxel grid in Cartesian space (Table 1) using a first order finite difference solver. A sufficiently large volume was used such that edge effects are negligible, with the condition being that $C_{Ca,cyt}$ did not exceed a level 1% above baseline at the

edges (excluding the edge containing the IP_3Rs), except where we intentionally simulated compressed cells. *The Courant-Freidcrichs-Lewy* condition:

$$\frac{2D_s dt}{dx^2} < 1$$

Equation 5

was obeyed for each species, where *dt* is the simulation time-step and *dx* is the linear size of a voxel. Simulation was conducted using bespoke C code employing Intel AVX-2 vector extensions. The Python language was used to process and analyze simulation results.

Boundary conditions

Our model was initialized with homogeneous Ca^{2+} and buffer concentrations as given in Table 1, with $C_{CaB,cyt}$ being initialized to equilibrium values. A zero flux boundary condition was applied to the edges of the cuboidal simulation volume.

Simulation verification

Our simulation code was compared with analytical expressions for simplified test cases of 3D diffusion from a point source and for the microdomain profile of an isolated Ca^{2+} source in a strongly buffered environment.

Analytical diffusion

Equation 6 gives the analytical form of the concentration profile for a slug of mass, *M*, released at position $r = 0$ and time $t = 0$, where *r* is scalar radius from the origin (Balluffi, 2005).

$$C(r,t) = \frac{M}{(4D\pi t)^{3/2}} \exp\left(-\frac{r^2}{4Dt}\right)$$

Equation 6

The Ca^{2+} diffusion component of our simulation was initialized with a volume of 1.68 μm on a side, with Ca^{2+} parameters as per Table 1, and with zero Ca^{2+} concentration except in the central

voxel, which was set to 1 molar. Fig 3A,B illustrates the good agreement between our simulation and the analytical case.

Analytical microdomain profile

An analytical solution for the equilibrium concentration profile, at distance r from an isolated source of constant current J_{Ca} in an isotropic, exists for an inexhaustible buffer that only forward binds:. This is known as the excess buffer approximation (Smith, 1996)

$$c(r) = c_\infty + \frac{J_{Ca}}{2\pi D_{ca}} \frac{e^{-r/\lambda}}{r}$$

Equation 7

where c_∞ is the Ca^{2+} concentration far from the source – that is the equilibrium level, $\gamma = (D\tau)^{0.5}$ is a space constant and $\tau = 1/(K_{on}B)$ is the mean capture time of the buffer, of concentration B. Our simulation was configured to match, as well as possible, this analytical case. Specifically parameters from Table 1 were used to simulate a single source, with the following modifications: K_{Off} was set to zero (forward binding only), $\phi_{B,cyt}$ from Equation 2 was set to zero (inexhaustible buffer) and the concentration gradient was removed from Equation 3 (constant current source). As a consequence of these changes any background Ca^{2+} was rapidly depleted in this model, so c_∞ was also set to zero to facilitate direct comparison. After running the model, the total quantity of free (unbuffered) cytosolic Ca^{2+} was examined (Fig 3C). This level rose rapidly, stabilizing to equilibrium in ~0.1ms. A comparison of Equation 6 and the concentration profile of the model, once equilibrium is reached, is shown in Fig 3. The responses were very similar, with the effect of quantized voxel sizes limiting the model concentration at small r and edge effects raising the concentration at high r.

Simulation Parameters

Parameters for the simulation were chosen to be physiologically relevant, and are given in Table 1 along with references.

Results

The GRIN microprobe was inserted easily into the lumen of an artery, (Fig 1) delivered a field-of-view of 0.5 mm diameter, and allowed a large number (~200) of naturally connected endothelial cells to be imaged (Fig 1I) with subcellular resolution (~4.5 μm; Fig 2D). In arteries pressurized to 60 mmHg, activation of the endothelium by extra-luminal acetylcholine (ACh; 100 μM applied to the chamber, ~1 μM estimated at the vessel lumen; 60 mmHg; Supplementary Movie S1&S2) evoked reproducible rises in cytoplasmic Ca^{2+} concentration ($[Ca^{2+}]_c$) in the majority of cells in the field (Fig 4A). The response was composed of temporally-distinct components. Initially, small spatial groupings of cells (macrodomain) activated (Fig 4A, Supplementary Movie S2) in small regions of the endothelium and from which waves expanded (Fig 4A) to recruit the remaining majority of cells in the field-of-view (Fig 4&5).

As a result of the wave progression there was a large spread of times to first Ca^{2+} response (latency) in various cells (Fig 4B-C left panels) which complicated summarizing and evaluating responses. Therefore, the temporal latency between individual Ca^{2+} traces (F/F_0) was removed by aligning the signals to each other (using the initial peak in the first derivative of each signal) (Fig 4B-C, middle panels). This procedure removed heterogeneity resulting from the time to onset of individual signals and provided a clearer illustration of total Ca^{2+} activity. Upon consecutive stimulation with ACh, the response, as measured from the number of cells activated and the average peak change in F/F_0, was approximately reproducible (Fig 4D, n = 5).

The Ca^{2+} rise evoked by ACh was approximately reproducible on successive application of ACh (Fig 4D; n = 5). The ACh-evoked Ca^{2+} rise persisted in a Ca^{2+}-free bathing solution (n=4) but was blocked by the SERCA inhibitor cyclopiazonic acid (10 μM; n=3) and the IP_3R blocker 2-aminoethoxydiphenyl borate (100 μM; n=3; Fig 6). Caffeine (10 mM; n=3) did not evoke a Ca^{2+} increase and the ACh-evoked Ca^{2+} rise was unaltered by ryanodine (10 μM; n=3). These results suggest that the Ca^{2+} rise originated from an IP_3-sensitive Ca^{2+} store and that RyRs play a minor role in Ca^{2+} signaling in the endothelium (Fig 6). The TRPV4 antagonist RN1734 (30 μM; 30 min) did not decrease ACh evoked endothelial response at 60 mmHg (Fig 6D) - as anticipated from previous findings in larger arteries (Hartmannsgruber *et al.*, 2007; Loot *et al.*, 2008).

Endothelial cells are stimulated almost constantly by extrinsic blood-borne bioactive molecules amid a background of hemodynamic mechanical forces. The combined effect of chemical activators and mechanical force is presumably incorporated into the endothelium's biological response, but details are largely unknown. We addressed whether a change in endothelium-dependent Ca^{2+} signaling, evoked by a bioactive molecule (ACh), occurs with variation in transmural pressure, and hence mechanical force. At 60 mmHg, ACh (100 μM) evoked asynchronous Ca^{2+} waves and oscillations that originated in macrodomains (Fig 7A; Supplementary Movie S2). As transmural pressure increased (60 to 110 to 160 mmHg), both the amplitude of the Ca^{2+} rise that occurred in each cell and the temporal spread of total activation decreased (Fig 7A-D; Supplementary Movie S3). The suppression of the amplitude of the Ca^{2+} signals reversed as pressure decreased (not shown). These results suggest that increased pressure in the intact artery suppressed IP_3-evoked Ca^{2+} signals. IP_3R itself is not reported to be stretch-sensitive and mechanical activation of IP_3-generating processes is unlikely to explain our observations as in transient increases in IP_3 production and IP_3-evoked Ca^{2+} release occur typically (Jena *et al.*, 1997).

The question arises as to how increased pressure suppressed IP_3-evoked Ca^{2+} signals. Significant changes in endothelial cell shape occurred with increased pressure (Fig 8). Increased circumferential stretch, with increased pressure, elongated cells around the artery and cell thickness was significantly decreased to maintain volume (Fig 8A,B). Increased transmural pressure may have also compressed the endothelial cells. The change in cell geometry is likely to alter Ca^{2+} dynamics in the endothelial cells at the microdomain level near IP_3R. The effect of changes in cell geometry on IP_3-evoked Ca^{2+} signals was therefore considered further. To explore the effects of changes in the cells geometry changes on IP_3-mediated Ca^{2+} release at the relevant scale, which exists below functional optical microscopy, we computationally simulated events at an IP_3R cluster.

IP_3R are arranged in clusters and the sensitivity of IP_3Rs to Ca^{2+} is such that the $[Ca^{2+}]_c$ in the microdomain of a single open IP_3R (or cluster) may be high enough to activate near-by IP_3Rs (or clusters)(Callamaras *et al.*, 1998). This process of Ca^{2+} activation may become regenerative and carry a wave of activity across cells (Fig 4&5). In the transmission process, IP_3R activity is exquisitely sensitive to distance between channels on the ER and to the cytosolic space between

the ER and membrane structures, such as mitochondria and the plasma membrane (McGeown *et al.*, 1996; Rizzuto *et al.*, 1998; Mazel *et al.*, 2009; Olson *et al.*, 2010; Olson *et al.*, 2012). These features (clustering, cytosolic space) create a local diffusive environment (i.e. microdomain) in which Ca^{2+} and Ca^{2+} buffers regulate the activity of IP_3Rs and the release of Ca^{2+} from the ER due to the local $[Ca^{2+}]_c$.

The opening of a single IP_3R introduced a point source of Ca^{2+} that equilibrated rapidly by diffusion and aggressive cytosolic buffering, to produce a localized, quasi-static region of elevated $[Ca^{2+}]_c$ (microdomain; Fig 9A,B) around the channel. The Ca^{2+} concentration decreased sharply with distance from the IP_3R with a characteristic scale (the distance at which $[Ca^{2+}]$ remains elevated by at least one order of magnitude) on the order of 100 nm (Fig 9B). The presence of many such point sources resulted in a greater $[Ca^{2+}]_c$ in the vicinity of IP_3R clusters than isolated receptors (Fig 9C). The raised $[Ca^{2+}]_c$ that occurred as a result of IP_3R clustering reduced the local ion gradient between the store ($[Ca^{2+}]_{ER}$) and the cytosol, and so reduced the entropic force driving Ca^{2+} release through the channel. In addition, the elevated $[Ca^{2+}]_c$ merged the microdomain of each IP_3R into a unified, larger domain with scales approaching the 500 nm thickness typical of endothelial cells.

In wide, thin cells (e.g. endothelium) IP_3Rs release Ca^{2+} into the cytosolic space between the ER and the cellular plasma membrane, where proximity of the IP_3R to the cellular plasma membrane may create a restricted environment limiting the diffusion of Ca^{2+}. The decreased cell height as a result of the change in cell shape (Fig 8) reduces the distance between the IP_3Rs and the opposing plasma membrane, restricting Ca^{2+} diffusion away from IP_3R and, as a result, increasing the $[Ca^{2+}]_c$ at the receptors (Fig 9A,C). Thus, the decreased height reduced the total Ca^{2+} liberated from the ER by reducing the entropic force driving Ca^{2+} release (Fig 9D). In this way, a mechanical force (circumferential stretch) can reduce Ca^{2+} release via IP_3R, in the absence of any force- or stretch-sensitive molecular machinery. Notably, the clustering of IP_3Rs extends this effect, when compared to isolated receptors, from sub 100 nm thick cells to those with a 100-500 nm thickness typical of the endothelium (Fig 9).

Discussion

The endothelium's control over cardiovascular structure and function requires cooperation among endothelial cells to both sense and communicate stimuli efficiently with itself and other cell types (Ledoux *et al.*, 2008; Behringer & Segal, 2012; Socha *et al.*, 2012b; Tran *et al.*, 2012; Qian *et al.*, 2013). The cooperative behavior is not well understood because of the difficulties in studying large numbers of endothelial cells in a physiological configuration. The miniature, wide-field GRIN imaging probe described permits endothelial Ca^{2+} activity from within an intact, pressurized artery to be observed. The microprobe bypasses the difficulties created by the artery wall in imaging blood vessels in a physiological configuration. Furthermore, the absence of biological tissue between the end of the probe and the endothelium minimized the light intensity required. The microprobe has a large depth-of-focus (141 μm) and delivers a 0.5 mm field of view to allow 200 cells to be viewed simultaneously.

The detection of chemical stimuli appears to be distributed among endothelial cells. In response to ACh, Ca^{2+} rises initiate in small regions of the endothelium and expand from these regions to recruit most of the cells in the field. The initiator regions (macrodomains) appear to be more sensitive to ACh. The path of the Ca^{2+} signal from the sensitive regions at times appeared poorly coordinated among endothelial cells - even chaotic. Nonetheless, the path and pattern were repeatable on successive application of ACh suggesting an encoded signal communicated among cells. The response to ACh was derived from an IP_3-mediated release of Ca^{2+} from the internal store. The Ca^{2+} rise persisted in a Ca^{2+}-free bath solution and was abolished by the SERCA pump inhibitor cyclopiazonic acid. The ACh-evoked Ca^{2+} rise persisted in ryanodine and caffeine failed to evoke a Ca^{2+} rise. However, release was inhibited by the IP_3R blocker 2-APB. The transmission of the Ca^{2+} signal among endothelial cells may involve Ca^{2+} or IP_3 or both.

In addition to receiving and communicating chemical stimuli, arteries are under permanent mechanical activation from shear stress and blood pressure. While cells often respond to the activation of mechanically-sensitive components (e.g. via shear-stress) with increased ion channel and cell activity, the mechanical response to pressure differs and endothelial activity is suppressed. For example, transient and chronic increases in pressure each inhibit endothelial nitric oxide-mediated vasodilation (Hishikawa *et al.*, 1992; De Bruyn *et al.*, 1994; Huang *et al.*, 1998; Paniagua *et al.*, 2000; Jurva *et al.*, 2006; Phillips *et al.*, 2011). How pressure may suppress

endothelial activity is unresolved but increased reactive oxygen species may contribute (Huang *et al.*, 1998; Vecchione *et al.*, 2009; Zhao *et al.*, 2015). Here we report that endothelial Ca^{2+} signaling is suppressed when pressure is elevated. The suppressed Ca^{2+} signaling will presumably result in reduced production of nitric oxide and reduced endothelium-dependent dilation (Hishikawa *et al.*, 1992; Sun *et al.*, 2001).

The sensing system(s) for detecting changes in pressure in the endothelium are poorly understood. Pressure-evoked mechanical *deactivation* of ion channels have been proposed to account for some physiological responses (Hoffman *et al.*, 2011; Bagher *et al.*, 2012). We propose that changes in cell shape may be sufficient to underlie the detection of pressure-dependent mechanical forces by the endothelium. The changes in geometric shape of the cell in response to pressure changes are substantial. Compression flattens the cell and circumferential stretch also flattens the cell as the height of endothelial cells is reduced to maintain volume. Such The changes in geometric shape of the cell will bring the endoplasmic reticulum and plasma membranes closer together and create a region of restricted diffusion (see also Hong *et al.*, 2008; Qi *et al.*, 2015). The region of restricted diffusion changes the local diffusive environment surrounding IP_3R clusters and results in a higher concentration of Ca^{2+} near the IP_3R microdomain. This higher concentration results in a reduced Ca^{2+} gradient between the store and the cytosol. As a result, the entropic force driving Ca^{2+} release is reduced and so the amplitude of IP_3-evoked Ca^{2+} signals is also reduced (Fig 10). Reduced IP_3-evoked Ca^{2+} release may explain the suppression of artery level endothelium-derived responses at high transmural pressure (De Bruyn *et al.*, 1994; Huang *et al.*, 1998; Paniagua *et al.*, 2000; Zhao *et al.*, 2015). A specific force- or stretch-sensitive component is not required but rather cell shape changes alter the local concentrations of second messengers (e.g. Ca^{2+}) within the cell to modulate the overall response of the cell.

The pressure-sensitive change in IP_3-evoked Ca^{2+} provides an additional level of complexity and subtly to mechanosensitive signalling which may induce several further signals to generate a functional response. For example, the changes in $[Ca^{2+}]_c$ as a result of geometric modulation of IP_3-evoke Ca^{2+} release may modulate the activity of plasma membrane located Ca^{2+}-sensitive ion channels to explain, at least in part, some contradictory observations of apparent mechanical activation (shear-stress Strotmann *et al.*, 2000; Alessandri-Haber *et al.*, 2003; Loukin *et al.*,

2010) and inhibition (pressure increases Bagher *et al.*, 2012) of ion channels. In the latter study, when pressure decreased from 80 mmHg to 5 mmHg, the frequency of transient localized endothelial Ca^{2+} rises increased (Bagher *et al.*, 2012). The authors attributed the Ca^{2+} changes to influx via TRPV4. The mechanosensor for the pressure-induced change in TRPV4 activity was unclear but the authors suggested reduced radial compression of endothelial cells may activate the channel (Bagher *et al.*, 2012). TRPV4 is Ca^{2+}-sensitive and activated by increases in $[Ca^{2+}]_c$ (Strotmann *et al.*, 2003). Interestingly, in their study (Bagher *et al.*, 2012) found the local endothelial Ca^{2+} events studied were blocked fully by a phospholipase C inhibitor (U-73122) and an IP_3R blocker (xestospongin C) almost abolished Ca^{2+} events at 80 mmHg significantly inhibited responses at 5 mmHg. These results suggest that IP_3-mediated Ca^{2+} release may contribute significantly to the spontaneous Ca^{2+} events. Geometric regulation of IP_3-evoked Ca^{2+} release may provide the pressure sensor for the change in TRPV4 activity.

Endothelial cells are acknowledged to be sensitive to their geometry and changes known to regulate proliferation and cell death (Chen *et al.*, 1997). Changes in cell shape alter tension in the cell membrane to modify separation of components within membranes (Sheetz, 1993; Mederos y Schnitzler *et al.*, 2008) with consequences for cell behavior (Mossman *et al.*, 2005). Alternatively, changes in links between the plasma membrane and cytoskeleton or mechanosensitive ion channels, may detect changes in membrane tension (Patel *et al.*, 2001). Several proteins also have domains (BAR- or ALPS-) found in membranes that are curved and may contribute to detecting cell shape changes. The extent of membrane binding of these protein domains changes with membrane curvature (Zhao *et al.*, 2011). The protein domains may either induce or are sensitive to membrane curvature (Zimmerberg & Kozlov, 2006). GEFs and GAPs with curvature sensing protein domains may alter the activity of GTPases in a tension-dependent manner (de Kreuk *et al.*, 2011) to explain geometry sensitivity of cells. We propose changes in cell geometry may also alter ion diffusional gradients which act then to sense stimuli and evoke vascular responses.

For normal function, cells in the vascular wall must act in a coordinated manner. The spatial relationships among extracellular chemical stimuli, cell architecture and Ca^{2+} signals are central to signal processing and the coordinated behavior. Indeed the macroscopic configuration of the intact endothelium is essential for physiological mechanotransduction events to occur although

'sensing' occurs on the microdomain scale. The detection of mechanical forces like pressure is critically dependent on the organization of the sensing proteins and the contact of cells with other cells. In other investigations on mechanotransduction, the same protein was found to evoke different responses when organized in 3D filaments rather than arranged on a flat surface (Cukierman *et al.*, 2001). Some types of mechanosensitivity seen in isolated single cells were lost when cells are in contact with one another (Yeung *et al.*, 2005). Our results in intact arteries in a physiological configuration suggest that mechanical activation by pressure is merged into the agonist evoked response in the endothelium. The pressure-dependence of Ca^{2+} release provides a mechanism for transmural pressure to be encoded and integrated to a common, coordinated output without imposing the requirement for mechanosensitivity on any of the molecular machinery in the signaling pathway. The time course of this response will be rapid and may form an early event in an altered mechanical environment. Our results also suggest how hypertensive conditions limit the ability of cells to engage in Ca^{2+} signaling, offering insight into the associated degeneration of endothelial response (Luscher & Vanhoutte, 1986; Wallace *et al.*, 2007) and the role that IP_3R clustering may play.

Competing interests

None

Author contributions

The manuscript was prepared and written with contributions from all authors. All authors approved the final version of the manuscript.

Funding

This work was funded by the Wellcome Trust (092292/Z/10/Z) and British Heart Foundation (PG/11/70/29086 and Research Excellence Award (Edinburgh/Durham University)) and EPSRC; their support is gratefully acknowledged.

Acknowledgements

REFERENCES

Alessandri-Haber N, Yeh JJ, Boyd AE, Parada CA, Chen X, Reichling DB & Levine JD. (2003). Hypotonicity induces TRPV4-mediated nociception in rat. *Neuron* **39,** 497-511.

Angus JA, Campbell GR, Cocks TM & Manderson JA. (1983). Vasodilatation by acetylcholine is endothelium-dependent: a study by sonomicrometry in canine femoral artery in vivo. *J Physiol* **344,** 209-222.

Bagher P, Beleznai T, Kansui Y, Mitchell R, Garland CJ & Dora KA. (2012). Low intravascular pressure activates endothelial cell TRPV4 channels, local Ca^{2+} events, and IKCa channels, reducing arteriolar tone. *Proc Natl Acad Sci U S A* **109,** 18174-18179.

Balluffi R, Allen, S., Carter, W. (2005). Kinetics of Materials. *John Wiley and Sons* 103.

Behringer EJ & Segal SS. (2012). Tuning electrical conduction along endothelial tubes of resistance arteries through Ca^{2+}-activated K^{+} channels. *Circ Res* **110,** 1311-1321.

Behringer EJ & Segal SS. (2015). Membrane potential governs calcium influx into microvascular endothelium: Integral role for muscarinic receptor activation. *J Physiol*.

Billaud M, Lohman AW, Johnstone SR, Biwer LA, Mutchler S & Isakson BE. (2014). Regulation of cellular communication by signaling microdomains in the blood vessel wall. *Pharmacological reviews* **66,** 513-569.

Bortolozzi M, Lelli A & Mammano F. (2008). Calcium microdomains at presynaptic active zones of vertebrate hair cells unmasked by stochastic deconvolution. *Cell Calcium* **44,** 158-168.

Bubolz AH, Mendoza SA, Zheng X, Zinkevich NS, Li R, Gutterman DD & Zhang DX. (2012). Activation of endothelial TRPV4 channels mediates flow-induced dilation in human coronary arterioles: role of Ca^{2+} entry and mitochondrial ROS signaling. *Am J Physiol Heart Circ Physiol* **302,** H634-642.

Callamaras N, Marchant JS, Sun XP & Parker I. (1998). Activation and co-ordination of $InsP_3$-mediated elementary Ca^{2+} events during global Ca^{2+} signals in Xenopus oocytes. *J Physiol* **509 (Pt 1),** 81-91.

Chataigneau T, Feletou M, Duhault J & Vanhoutte PM. (1998a). Epoxyeicosatrienoic acids, potassium channel blockers and endothelium-dependent hyperpolarization in the guinea-pig carotid artery. *Br J Pharmacol* **123,** 574-580.

Chataigneau T, Feletou M, Thollon C, Villeneuve N, Vilaine JP, Duhault J & Vanhoutte PM. (1998b). Cannabinoid CB1 receptor and endothelium-dependent hyperpolarization in guinea-pig carotid, rat mesenteric and porcine coronary arteries. *Br J Pharmacol* **123,** 968-974.

Chen CS, Mrksich M, Huang S, Whitesides GM & Ingber DE. (1997). Geometric control of cell life and death. *Science* **276,** 1425-1428.

Chien S. (2007). Mechanotransduction and endothelial cell homeostasis: the wisdom of the cell. *Am J Physiol Heart Circ Physiol* **292,** H1209-1224.

Corey DP, Garcia-Anoveros J, Holt JR, Kwan KY, Lin SY, Vollrath MA, Amalfitano A, Cheung EL, Derfler BH, Duggan A, Geleoc GS, Gray PA, Hoffman MP, Rehm HL, Tamasauskas D & Zhang DS. (2004). TRPA1 is a candidate for the mechanosensitive transduction channel of vertebrate hair cells. *Nature* **432,** 723-730.

Craig J & Martin W. (2012). Dominance of flow-mediated constriction over flow-mediated dilatation in the rat carotid artery. *Br J Pharmacol* **167,** 527-536.

Cukierman E, Pankov R, Stevens DR & Yamada KM. (2001). Taking cell-matrix adhesions to the third dimension. *Science* **294,** 1708-1712.

De Bruyn VH, Nuno DW, Cappelli-Bigazzi M, Dole WP & Lamping KG. (1994). Effect of acute hypertension in the coronary circulation: role of mechanical factors and oxygen radicals. *J Hypertens* **12,** 163-172.

de Kreuk BJ, Nethe M, Fernandez-Borja M, Anthony EC, Hensbergen PJ, Deelder AM, Plomann M & Hordijk PL. (2011). The F-BAR domain protein PACSIN2 associates with Rac1 and regulates cell spreading and migration. *J Cell Sci* **124,** 2375-2388.

Deanfield JE, Halcox JP & Rabelink TJ. (2007). Endothelial function and dysfunction: testing and clinical relevance. *Circulation* **115,** 1285-1295.

Dedman A, Sharif-Naeini R, Folgering JH, Duprat F, Patel A & Honore E. (2009). The mechano-gated K(2P) channel TREK-1. *Eur Biophys J* **38,** 293-303.

Dunn WR, Wellman GC & Bevan JA. (1994). Enhanced resistance artery sensitivity to agonists under isobaric compared with isometric conditions. *Am J Physiol* **266,** H147-155.

Duza T & Sarelius IH. (2004). Localized transient increases in endothelial cell Ca^{2+} in arterioles in situ: implications for coordination of vascular function. *Am J Physiol Heart Circ Physiol* **286,** H2322-2331.

Earley S & Brayden JE. (2015). Transient receptor potential channels in the vasculature. *Physiol Rev* **95,** 645-690.

Edelstein A, Amodaj N, Hoover K, Vale R & Stuurman N. (2010). Computer control of microscopes using microManager. *Current protocols in molecular biology / edited by Frederick M Ausubel [et al]* **Chapter 14,** Unit14 20.

Falcone JC, Kuo L & Meininger GA. (1993). Endothelial cell calcium increases during flow-induced dilation in isolated arterioles. *Am J Physiol* **264,** H653-659.

Faraci FM & Heistad DD. (1990). Regulation of large cerebral arteries and cerebral microvascular pressure. *Circ Res* **66,** 8-17.

Faraci FM, Orgren K & Heistad DD. (1994). Impaired relaxation of the carotid artery during activation of ATP-sensitive potassium channels in atherosclerotic monkeys. *Stroke* **25,** 178-182.

Fischer MJ, Uchida S & Messlinger K. (2010). Measurement of meningeal blood vessel diameter in vivo with a plug-in for ImageJ. *Microvascular research* **80,** 258-266.

Flusberg BA, Nimmerjahn A, Cocker ED, Mukamel EA, Barretto RP, Ko TH, Burns LD, Jung JC & Schnitzer MJ. (2008). High-speed, miniaturized fluorescence microscopy in freely moving mice. *Nat Methods* **5,** 935-938.

Francis M, Qian X, Charbel C, Ledoux J, Parker JC & Taylor MS. (2012). Automated region of interest analysis of dynamic Ca(2)+ signals in image sequences. *Am J Physiol Cell Physiol* **303,** C236-243.

Gunduz F, Meiselman HJ & Baskurt OK. (2008). High intravascular pressure attenuates vascular dilation responses of small mesenteric arteries in the rat. *Circulation journal : official journal of the Japanese Circulation Society* **72,** 482-486.

Hartmannsgruber V, Heyken WT, Kacik M, Kaistha A, Grgic I, Harteneck C, Liedtke W, Hoyer J & Kohler R. (2007). Arterial response to shear stress critically depends on endothelial TRPV4 expression. *PLoS One* **2,** e827.

Hishikawa K, Nakaki T, Suzuki H, Saruta T & Kato R. (1992). Transmural pressure inhibits nitric oxide release from human endothelial cells. *Eur J Pharmacol* **215,** 329-331.

Hoffman BD, Grashoff C & Schwartz MA. (2011). Dynamic molecular processes mediate cellular mechanotransduction. *Nature* **475,** 316-323.

Hong D, Jaron D, Buerk DG & Barbee KA. (2008). Transport-dependent calcium signaling in spatially segregated cellular caveolar domains. *Am J Physiol Cell Physiol* **294,** C856-866.

Huang A, Sun D, Kaley G & Koller A. (1998). Superoxide released to high intra-arteriolar pressure reduces nitric oxide-mediated shear stress- and agonist-induced dilations. *Circ Res* **83,** 960-965.

Huang TY, Chu TF, Chen HI & Jen CJ. (2000). Heterogeneity of $[Ca^{2+}]i$ signaling in intact rat aortic endothelium. *FASEB J* **14,** 797-804.

Janssen DA, Hoenderop JG, Jansen KC, Kemp AW, Heesakkers JP & Schalken JA. (2011). The mechanoreceptor TRPV4 is localized in adherence junctions of the human bladder urothelium: a morphological study. *J Urol* **186,** 1121-1127.

Jena M, Minore JF & O'Neill WC. (1997). A volume-sensitive, IP_3-insensitive Ca^{2+} store in vascular endothelial cells. *Am J Physiol* **273,** C316-322.

Jurva JW, Phillips SA, Syed AQ, Syed AY, Pitt S, Weaver A & Gutterman DD. (2006). The effect of exertional hypertension evoked by weight lifting on vascular endothelial function. *J Am Coll Cardiol* **48,** 588-589.

Kim P, Chung E, Yamashita H, Hung KE, Mizoguchi A, Kucherlapati R, Fukumura D, Jain RK & Yun SH. (2010). In vivo wide-area cellular imaging by side-view endomicroscopy. *Nat Methods* **7,** 303-305.

Knudsen HL & Frangos JA. (1997). Role of cytoskeleton in shear stress-induced endothelial nitric oxide production. *Am J Physiol* **273,** H347-355.

Kohler R, Heyken WT, Heinau P, Schubert R, Si H, Kacik M, Busch C, Grgic I, Maier T & Hoyer J. (2006). Evidence for a functional role of endothelial transient receptor potential V4 in shear stress-induced vasodilatation. *Arterioscler Thromb Vasc Biol* **26,** 1495-1502.

Kusche-Vihrog K, Jeggle P & Oberleithner H. (2014). The role of ENaC in vascular endothelium. *Pflugers Arch* **466,** 851-859.

Lamping KG & Faraci FM. (2001). Role of sex differences and effects of endothelial NO synthase deficiency in responses of carotid arteries to serotonin. *Arterioscler Thromb Vasc Biol* **21,** 523-528.

Ledoux J, Taylor MS, Bonev AD, Hannah RM, Solodushko V, Shui B, Tallini Y, Kotlikoff MI & Nelson MT. (2008). Functional architecture of inositol 1,4,5-trisphosphate signaling in restricted spaces of myoendothelial projections. *Proc Natl Acad Sci U S A* **105,** 9627-9632.

Li J, Hou B, Tumova S, Muraki K, Bruns A, Ludlow MJ, Sedo A, Hyman AJ, McKeown L, Young RS, Yuldasheva NY, Majeed Y, Wilson LA, Rode B, Bailey MA, Kim HR, Fu Z, Carter DA, Bilton J, Imrie H, Ajuh P, Dear TN, Cubbon RM, Kearney MT, Prasad RK, Evans PC, Ainscough JF & Beech DJ. (2014). Piezo1 integration of vascular architecture with physiological force. *Nature*.

Loot AE, Popp R, Fisslthaler B, Vriens J, Nilius B & Fleming I. (2008). Role of cytochrome P450-dependent transient receptor potential V4 activation in flow-induced vasodilatation. *Cardiovasc Res* **80,** 445-452.

Loukin S, Zhou X, Su Z, Saimi Y & Kung C. (2010). Wild-type and brachyolmia-causing mutant TRPV4 channels respond directly to stretch force. *J Biol Chem* **285,** 27176-27181.

Luscher TF & Vanhoutte PM. (1986). Endothelium-dependent contractions to acetylcholine in the aorta of the spontaneously hypertensive rat. *Hypertension* **8,** 344-348.

Marchenko SM & Sage SO. (2000). Effects of shear stress on [Ca^{2+}]i and membrane potential of vascular endothelium of intact rat blood vessels. *Exp Physiol* **85,** 43-48.

Maroto R, Raso A, Wood TG, Kurosky A, Martinac B & Hamill OP. (2005). TRPC1 forms the stretch-activated cation channel in vertebrate cells. *Nat Cell Biol* **7,** 179-185.

Mazel T, Raymond R, Raymond-Stintz M, Jett S & Wilson BS. (2009). Stochastic modeling of calcium in 3D geometry. *Biophys J* **96,** 1691-1706.

McCarron JG, Chalmers S, MacMillan D & Olson ML. (2010). Agonist-evoked Ca^{2+} wave progression requires Ca^{2+} and IP_3. *J Cell Physiol* **224,** 334-344.

McGeown JG, Drummond RM, McCarron JG & Fay FS. (1996). The temporal profile of calcium transients in voltage clamped gastric myocytes from Bufo marinus. *J Physiol* **497 (Pt 2),** 321-336.

Mchedlishvili g. (1986). Arterial Behavior and Blood Circulation in the Brain. *New York, Plenum Publishing Corp,* .

Means S, Smith AJ, Shepherd J, Shadid J, Fowler J, Wojcikiewicz RJ, Mazel T, Smith GD & Wilson BS. (2006). Reaction diffusion modeling of calcium dynamics with realistic ER geometry. *Biophys J* **91,** 537-557.

Mederos y Schnitzler M, Storch U, Meibers S, Nurwakagari P, Breit A, Essin K, Gollasch M & Gudermann T. (2008). Gq-coupled receptors as mechanosensors mediating myogenic vasoconstriction. *EMBO J* **27,** 3092-3103.

Mendoza SA, Fang J, Gutterman DD, Wilcox DA, Bubolz AH, Li R, Suzuki M & Zhang DX. (2010). TRPV4-mediated endothelial Ca^{2+} influx and vasodilation in response to shear stress. *Am J Physiol Heart Circ Physiol* **298,** H466-476.

Moccia F, Berra-Romani R & Tanzi F. (2012). Update on vascular endothelial Ca^{2+} signalling: A tale of ion channels, pumps and transporters. *World journal of biological chemistry* **3,** 127-158.

Mossman KD, Campi G, Groves JT & Dustin ML. (2005). Altered TCR signaling from geometrically repatterned immunological synapses. *Science* **310,** 1191-1193.

Muller JM, Davis MJ, Kuo L & Chilian WM. (1999). Changes in coronary endothelial cell Ca^{2+} concentration during shear stress- and agonist-induced vasodilation. *Am J Physiol* **276,** H1706-1714.

Ohashi M, Faraci F & Heistad D. (2005). Peroxynitrite hyperpolarizes smooth muscle and relaxes internal carotid artery in rabbit via ATP-sensitive K^+ channels. *Am J Physiol Heart Circ Physiol* **289,** H2244-2250.

Olson ML, Chalmers S & McCarron JG. (2010). Mitochondrial Ca^{2+} uptake increases Ca^{2+} release from inositol 1,4,5-trisphosphate receptor clusters in smooth muscle cells. *J Biol Chem* **285,** 2040-2050.

Olson ML, Sandison ME, Chalmers S & McCarron JG. (2012). Microdomains of muscarinic acetylcholine and Ins(1,4,5)P_3 receptors create 'Ins(1,4,5)P_3 junctions' and sites of Ca^{2+} wave initiation in smooth muscle. *J Cell Sci* **125,** 5315-5328.

Paniagua OA, Bryant MB & Panza JA. (2000). Transient hypertension directly impairs endothelium-dependent vasodilation of the human microvasculature. *Hypertension* **36,** 941-944.

Patel AJ, Lazdunski M & Honore E. (2001). Lipid and mechano-gated 2P domain K^+ channels. *Curr Opin Cell Biol* **13,** 422-428.

Phillips SA, Das E, Wang J, Pritchard K & Gutterman DD. (2011). Resistance and aerobic exercise protects against acute endothelial impairment induced by a single exposure to hypertension during exertion. *Journal of applied physiology* **110,** 1013-1020.

Plane F, Wiley KE, Jeremy JY, Cohen RA & Garland CJ. (1998). Evidence that different mechanisms underlie smooth muscle relaxation to nitric oxide and nitric oxide donors in the rabbit isolated carotid artery. *Br J Pharmacol* **123,** 1351-1358.

Popp R, Fleming I & Busse R. (1998). Pulsatile stretch in coronary arteries elicits release of endothelium-derived hyperpolarizing factor: a modulator of arterial compliance. *Circ Res* **82,** 696-703.

Qi H, Li L & Shuai J. (2015). Optimal microdomain crosstalk between endoplasmic reticulum and mitochondria for Ca2+ oscillations. *Scientific reports* **5,** 7984.

Qian X, Francis M, Solodushko V, Earley S & Taylor MS. (2013). Recruitment of dynamic endothelial Ca2+ signals by the TRPA1 channel activator AITC in rat cerebral arteries. *Microcirculation* **20,** 138-148.

Ranade SS, Qiu Z, Woo SH, Hur SS, Murthy SE, Cahalan SM, Xu J, Mathur J, Bandell M, Coste B, Li YS, Chien S & Patapoutian A. (2014). Piezo1, a mechanically activated ion channel, is required for vascular development in mice. *Proc Natl Acad Sci U S A* **111,** 10347-10352.

Rizzuto R, Pinton P, Carrington W, Fay FS, Fogarty KE, Lifshitz LM, Tuft RA & Pozzan T. (1998). Close contacts with the endoplasmic reticulum as determinants of mitochondrial Ca^{2+} responses. *Science* **280,** 1763-1766.

Saunter CD, Semprini S, Buckley C, Mullins J & Girkin JM. (2012). Micro-endoscope for in vivo widefield high spatial resolution fluorescent imaging. *Biomedical optics express* **3,** 1274-1278.

Schindelin J, Arganda-Carreras I, Frise E, Kaynig V, Longair M, Pietzsch T, Preibisch S, Rueden C, Saalfeld S, Schmid B, Tinevez JY, White DJ, Hartenstein V, Eliceiri K, Tomancak P & Cardona A. (2012). Fiji: an open-source platform for biological-image analysis. *Nat Methods* **9,** 676-682.

Sheetz MP. (1993). Glycoprotein motility and dynamic domains in fluid plasma membranes. *Annual review of biophysics and biomolecular structure* **22,** 417-431.

Shiu YT, Li S, Marganski WA, Usami S, Schwartz MA, Wang YL, Dembo M & Chien S. (2004). Rho mediates the shear-enhancement of endothelial cell migration and traction force generation. *Biophys J* **86,** 2558-2565.

Smith GD. (1996). Analytical steady-state solution to the rapid buffering approximation near an open Ca^{2+} channel. *Biophys J* **71,** 3064-3072.

Socha MJ, Behringer EJ & Segal SS. (2012a). Calcium and electrical signalling along endothelium of the resistance vasculature. *Basic & clinical pharmacology & toxicology* **110,** 80-86.

Socha MJ, Domeier TL, Behringer EJ & Segal SS. (2012b). Coordination of intercellular Ca^{2+} signaling in endothelial cell tubes of mouse resistance arteries. *Microcirculation* **19,** 757-770.

Sonkusare SK, Bonev AD, Ledoux J, Liedtke W, Kotlikoff MI, Heppner TJ, Hill-Eubanks DC & Nelson MT. (2012). Elementary Ca^{2+} signals through endothelial TRPV4 channels regulate vascular function. *Science* **336,** 597-601.

Spassova MA, Hewavitharana T, Xu W, Soboloff J & Gill DL. (2006). A common mechanism underlies stretch activation and receptor activation of TRPC6 channels. *Proc Natl Acad Sci U S A* **103,** 16586-16591.

Strotmann R, Harteneck C, Nunnenmacher K, Schultz G & Plant TD. (2000). OTRPC4, a nonselective cation channel that confers sensitivity to extracellular osmolarity. *Nat Cell Biol* **2,** 695-702.

Strotmann R, Schultz G & Plant TD. (2003). Ca^{2+}-dependent potentiation of the nonselective cation channel TRPV4 is mediated by a C-terminal calmodulin binding site. *J Biol Chem* **278,** 26541-26549.

Sun D, Huang A, Recchia FA, Cui Y, Messina EJ, Koller A & Kaley G. (2001). Nitric oxide-mediated arteriolar dilation after endothelial deformation. *Am J Physiol Heart Circ Physiol* **280,** H714-721.

Tanko LB, Mikkelsen EO & Simonsen U. (1999). A new experimental approach in endothelium-dependent pharmacological investigations on isolated porcine coronary arteries mounted for impedance planimetry. *Br J Pharmacol* **128,** 165-173.

Thi MM, Tarbell JM, Weinbaum S & Spray DC. (2004). The role of the glycocalyx in reorganization of the actin cytoskeleton under fluid shear stress: a "bumper-car" model. *Proc Natl Acad Sci U S A* **101,** 16483-16488.

Toda N, Inoue S, Okunishi H & Okamura T. (1990). Intra- and extraluminally-applied acetylcholine on the vascular tone or the response to transmural stimulation in dog isolated mesenteric arteries. *Naunyn-Schmiedeberg's archives of pharmacology* **341,** 30-36.

Toda N, Minami Y & Onoue H. (1988). Extraluminally applied acetylcholine and oxyhemoglobin on the release and action of EDRF. *Eur J Pharmacol* **151,** 123-126.

Tran CH, Taylor MS, Plane F, Nagaraja S, Tsoukias NM, Solodushko V, Vigmond EJ, Furstenhaupt T, Brigdan M & Welsh DG. (2012). Endothelial Ca^{2+} wavelets and the induction of myoendothelial feedback. *Am J Physiol Cell Physiol* **302,** C1226-1242.

Tu H, Wang Z, Nosyreva E, De Smedt H & Bezprozvanny I. (2005). Functional characterization of mammalian inositol 1,4,5-trisphosphate receptor isoforms. *Biophys J* **88,** 1046-1055.

Tzima E, Irani-Tehrani M, Kiosses WB, Dejana E, Schultz DA, Engelhardt B, Cao G, DeLisser H & Schwartz MA. (2005). A mechanosensory complex that mediates the endothelial cell response to fluid shear stress. *Nature* **437,** 426-431.

Vecchione C, Carnevale D, Di Pardo A, Gentile MT, Damato A, Cocozza G, Antenucci G, Mascio G, Bettarini U, Landolfi A, Iorio L, Maffei A & Lembo G. (2009). Pressure-induced vascular oxidative stress is mediated through activation of integrin-linked kinase 1/betaPIX/Rac-1 pathway. *Hypertension* **54,** 1028-1034.

Wallace SM, Yasmin, McEniery CM, Maki-Petaja KM, Booth AD, Cockcroft JR & Wilkinson IB. (2007). Isolated systolic hypertension is characterized by increased aortic stiffness and endothelial dysfunction. *Hypertension* **50,** 228-233.

Yamamoto K, Sokabe T, Matsumoto T, Yoshimura K, Shibata M, Ohura N, Fukuda T, Sato T, Sekine K, Kato S, Isshiki M, Fujita T, Kobayashi M, Kawamura K, Masuda H, Kamiya A & Ando J. (2006). Impaired flow-dependent control of vascular tone and remodeling in P2X4-deficient mice. *Nat Med* **12,** 133-137.

Yeung T, Georges PC, Flanagan LA, Marg B, Ortiz M, Funaki M, Zahir N, Ming W, Weaver V & Janmey PA. (2005). Effects of substrate stiffness on cell morphology, cytoskeletal structure, and adhesion. *Cell motility and the cytoskeleton* **60,** 24-34.

Zhao H, Pykalainen A & Lappalainen P. (2011). I-BAR domain proteins: linking actin and plasma membrane dynamics. *Curr Opin Cell Biol* **23,** 14-21.

Zhao Y, Flavahan S, Leung SW, Xu A, Vanhoutte PM & Flavahan NA. (2015). Elevated pressure causes endothelial dysfunction in mouse carotid arteries by increasing local angiotensin signaling. *Am J Physiol Heart Circ Physiol* **308,** H358-363.

Zimmerberg J & Kozlov MM. (2006). How proteins produce cellular membrane curvature. *Nat Rev Mol Cell Biol* **7,** 9-19.

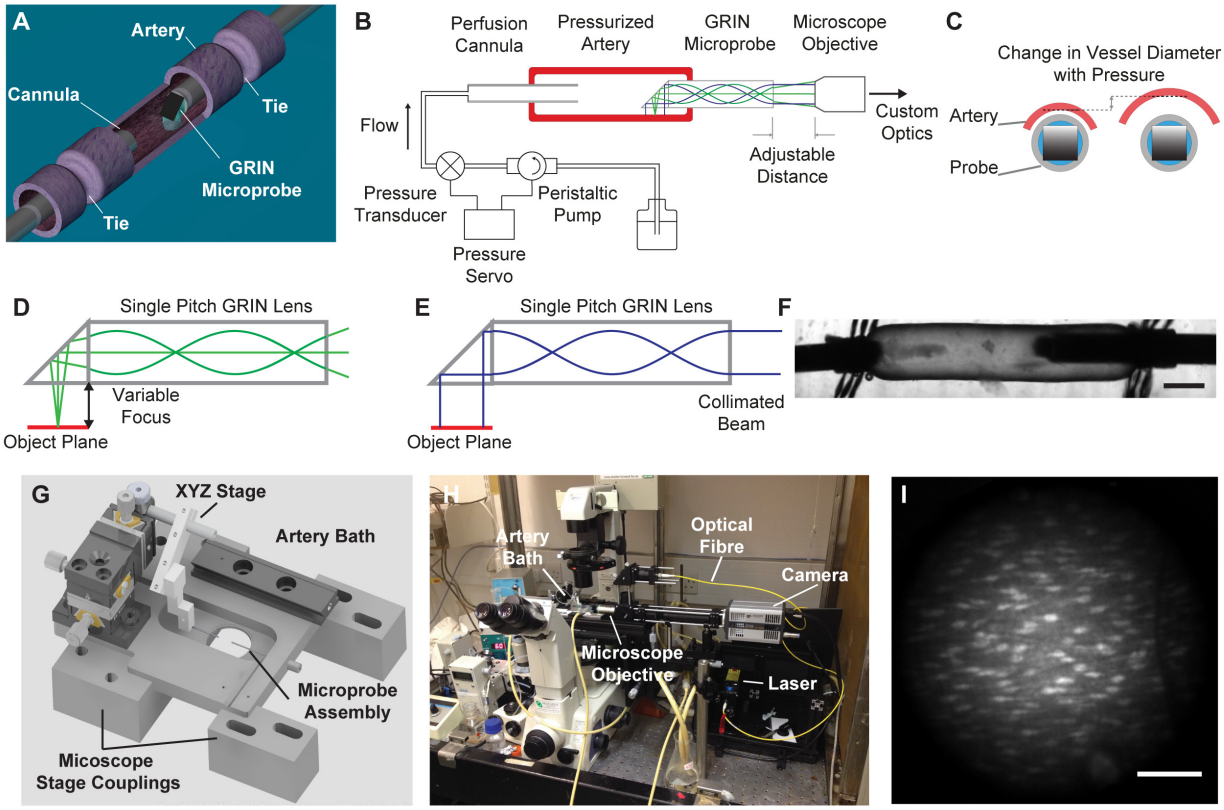

Figure 1. Endothelial GRIN imaging system (A) Cartoon showing the GRIN microprobe assembly inside a pressurized artery and endothelium (B), A simplified schematic diagram of the GRIN imaging system and the cannulated, pressurized artery. Focusing into the GRIN microprobe with a conventional microscope objective extended the image plane beyond the front surface of the prism and onto the endothelium. The connecting perfusion cannula (B) and pressure servo system permits intraluminal pressure to be controlled and the probe can be refocused if the artery position moves (C). (D) Schematic illustrating the optical emission path through the GRIN microprobe. The GRIN lens recongugates the image plane of a conventional microscope through the length of the cylinder. (E) Schematic illustrating the optical excitation path through the GRIN microprobe. The collimated input excitation light is re-collimated at the output of the GRIN lens. (F) A transmission image of a cannulated artery shows the GRIN microprobe on the right-hand side. (G) 3-dimensional rendering of the custom pressure arteriograph showing the position of the GRIN microprobe assembly and XYZ translation stage for positioning the artery. (H) Picture of setup during live imaging showing the camera and laser arrangement. (I) Fluorescence image of the endothelium visualized using the GRIN imaging system showing some activated cells (see Supplementary Movie S1). Note the field-of-view is circular due to the cross-sectional shape of the GRIN lens. Scale bar 100 µm.

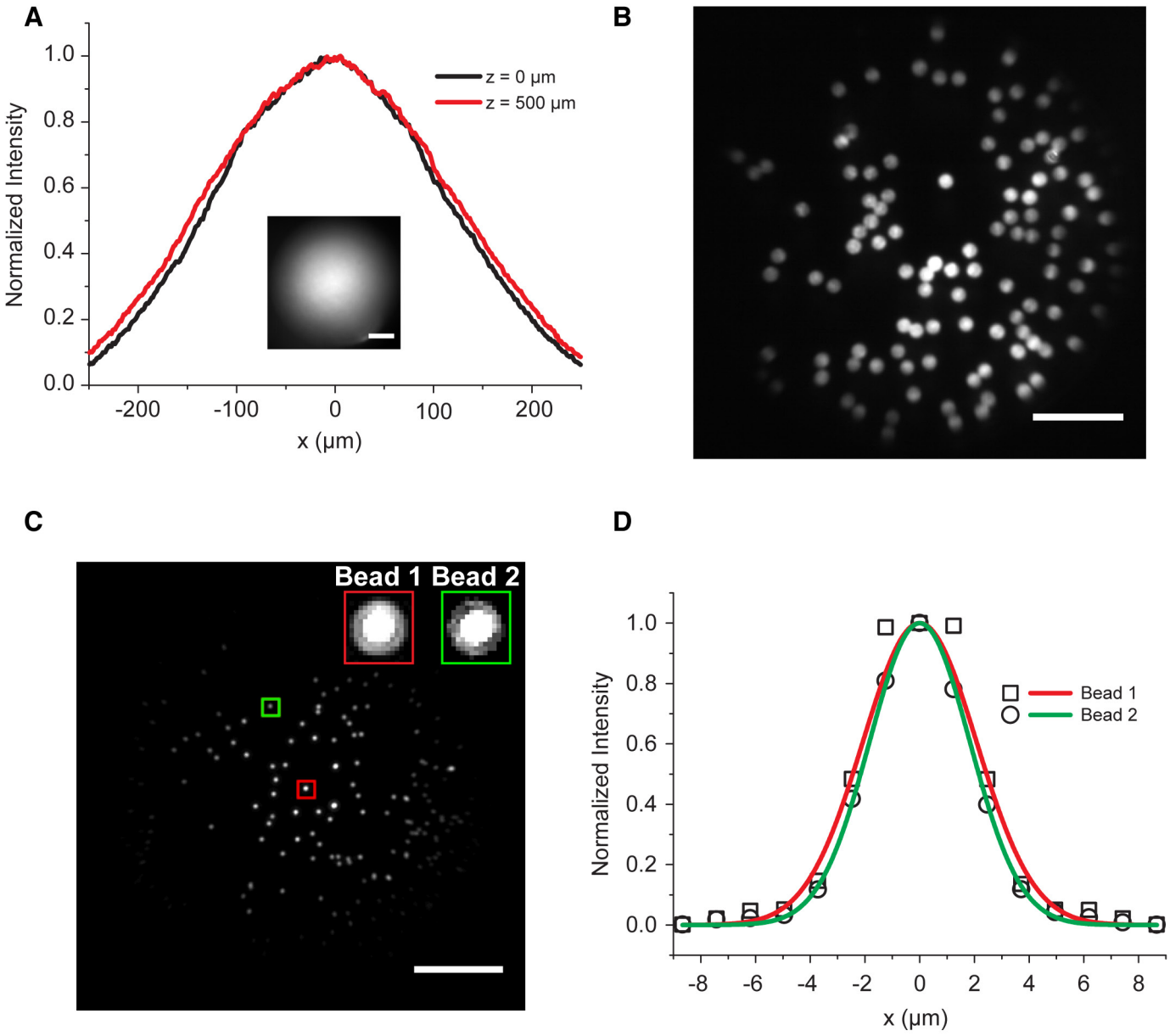

Figure 2. Optical characterization of the side-viewing GRIN imaging system. (A) Normalized intensity profiles, plotted as a function of radius (x) from the center of the circular cross-section of the GRIN lens, of images of fluorescein solution (1 μM) taken with the GRIN microendoscope as the focus was translated along the z-axis. (B) Fluorescence image of 15 μm fluorescent spheres. (C) Raw image of sub-resolution (1.0 μm) fluorescent beads obtained with the microendoscopic imaging system. Vignetting and heterogeneous fluorescence emission from the beads themselves result in apparent variation in size. By rescaling the intensity of the image (insets), beads of apparently different diameter, are shown to be approximately equal in size. (D) Normalized fluorescence intensity profiles, with Gaussian curves fitted, of the two beads highlighted in A. From such intensity profiles, we calculated the optical resolution of our system to be 4.51 ± 0.04 μm (n = 6 beads). Scale bars: 100 μm.

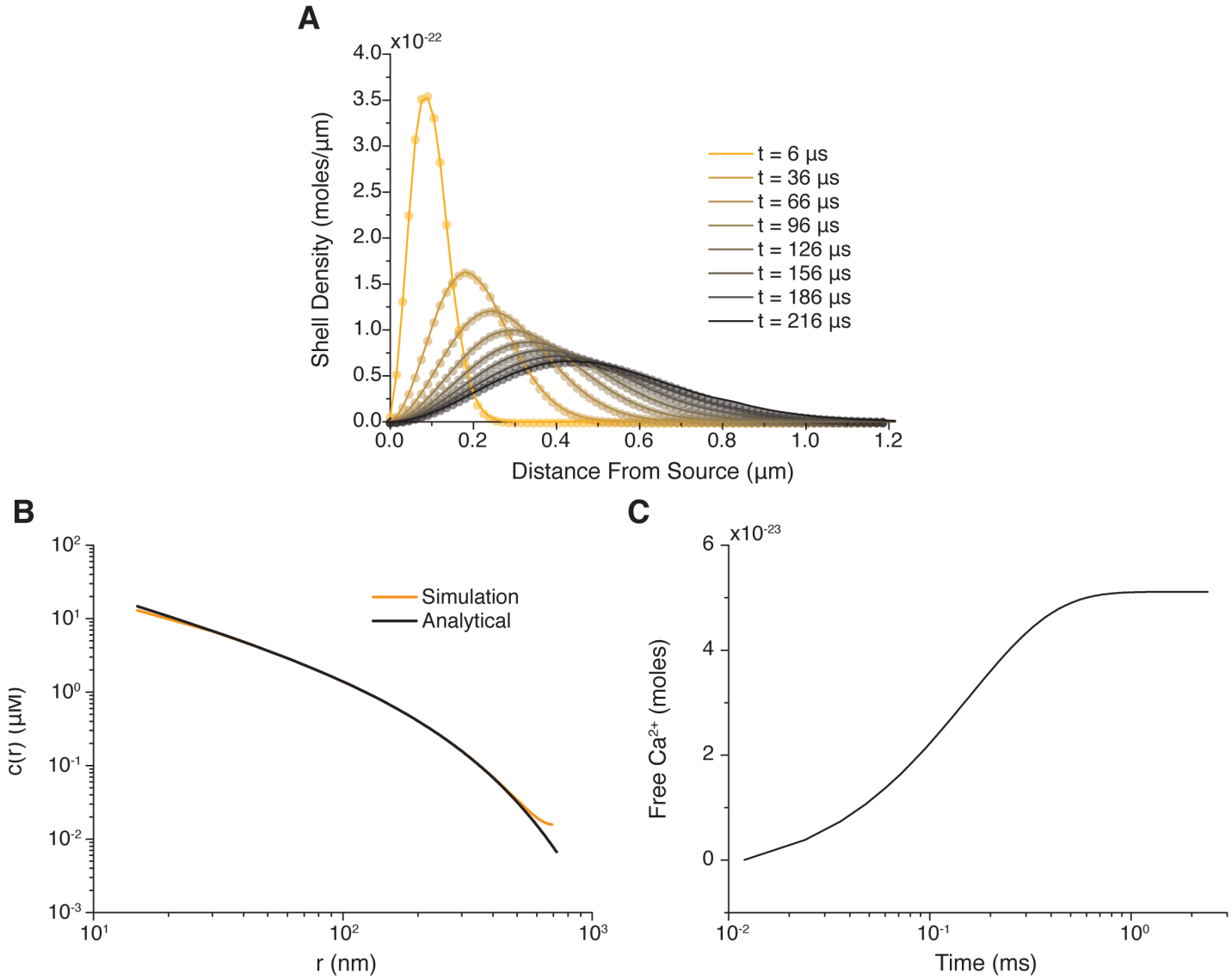

Figure 3. IP_3-evoked Ca^{2+} release simulation (A) Shell density plotted against distance from source (i.e. IP_3R). Theoretical (analytical test case; lines) plots of shell density for a slug of mass released at the origin shows good agreement with our simulated results (circles). (B) Ca^{2+} concentration as a function of radial distance from IP_3Rs. When equilibrated, the Ca^{2+} profile may be approximated by an analytical case (black line), which compares accurately to an examination of our simulation (yellow line). (C) Free Ca^{2+} concentration at an IP_3R as a function of time from receptor opening. The total cytosolic Ca^{2+} rises immediately after IP_3R opening then plateaus as the current flowing through IP_3R and cytosolic Ca^{2+} buffering reaches equilibrium (~0.1ms). See Methods section and Table 1 for equations, source references and parameters used to generate the figures.

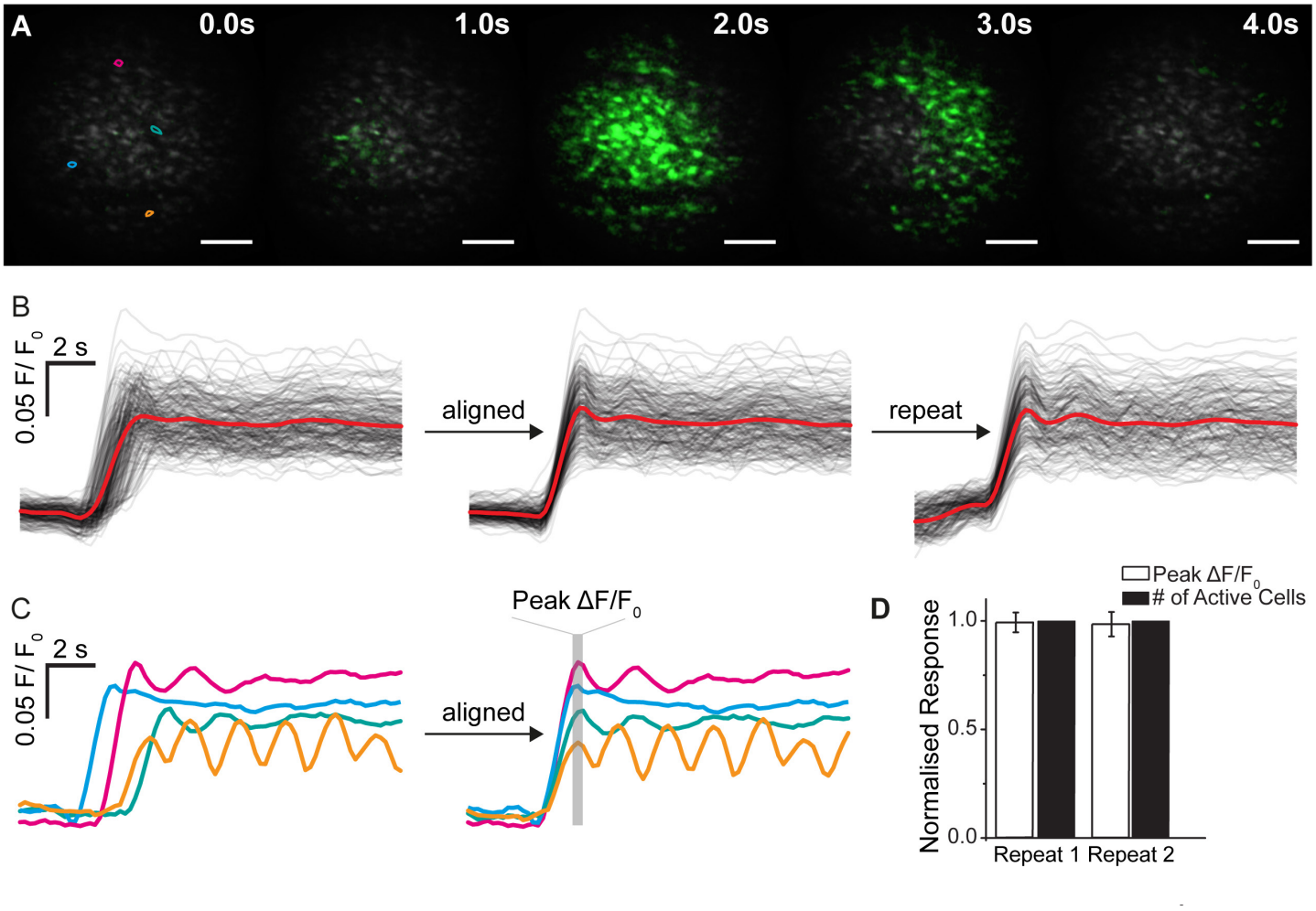

Figure 4. Endothelial Ca^{2+} imaging in intact, pressurized (60 mmHg) arteries. (A) Time-series Ca^{2+} images of endothelial cells showing the progression of the Ca^{2+} response evoked by ACh (100 µM; bath applied; ~1 µM estimated at the vessel lumen) recorded at 60 mmHg. Images are composed of instantaneous Ca^{2+} activity (green) overlaid on standard deviation images (grayscale) indicative of total Ca^{2+} activity. The rise began in a distinct cluster of cells (see 1 s) and progressed from there. Each bright spot is an individual cell. Scale bar: 100 µm. (B) ACh-evoked Ca^{2+} signals from the same cells shown in A. In the *left-panel* (unaligned data) the range of times for Ca^{2+} to increase for each of the ~200 cells is approximately 4 seconds. The spread of responses resulted in mean data representing the data poorly. The position of the first peak of derivative signals was used to align Ca^{2+} signals. This procedure synchronizes the Ca^{2+} rises occurring in each due to the action of ACh (*middle panel* 'aligned') and illustrates total Ca^{2+} activity (thick red line) with increased clarity. On successive application of ACh (20 minute reequilibration following wash), the response to ACh was reproducible (right panel). (C) Select examples of unaligned (left) and aligned (right) cellular Ca^{2+} responses from ROIs shown in (A). The gray box illustrates the time point of measurements from aligned signals. (D) Summary data illustrating the reproducibility of Ca^{2+} responses upon repeat application (wash + 20 minute reequilibration) with ACh. Data are presented as mean ± SEM and normalized to control (n = 5; first ACh application, 1; not shown), $p < 0.05$ was considered significant.

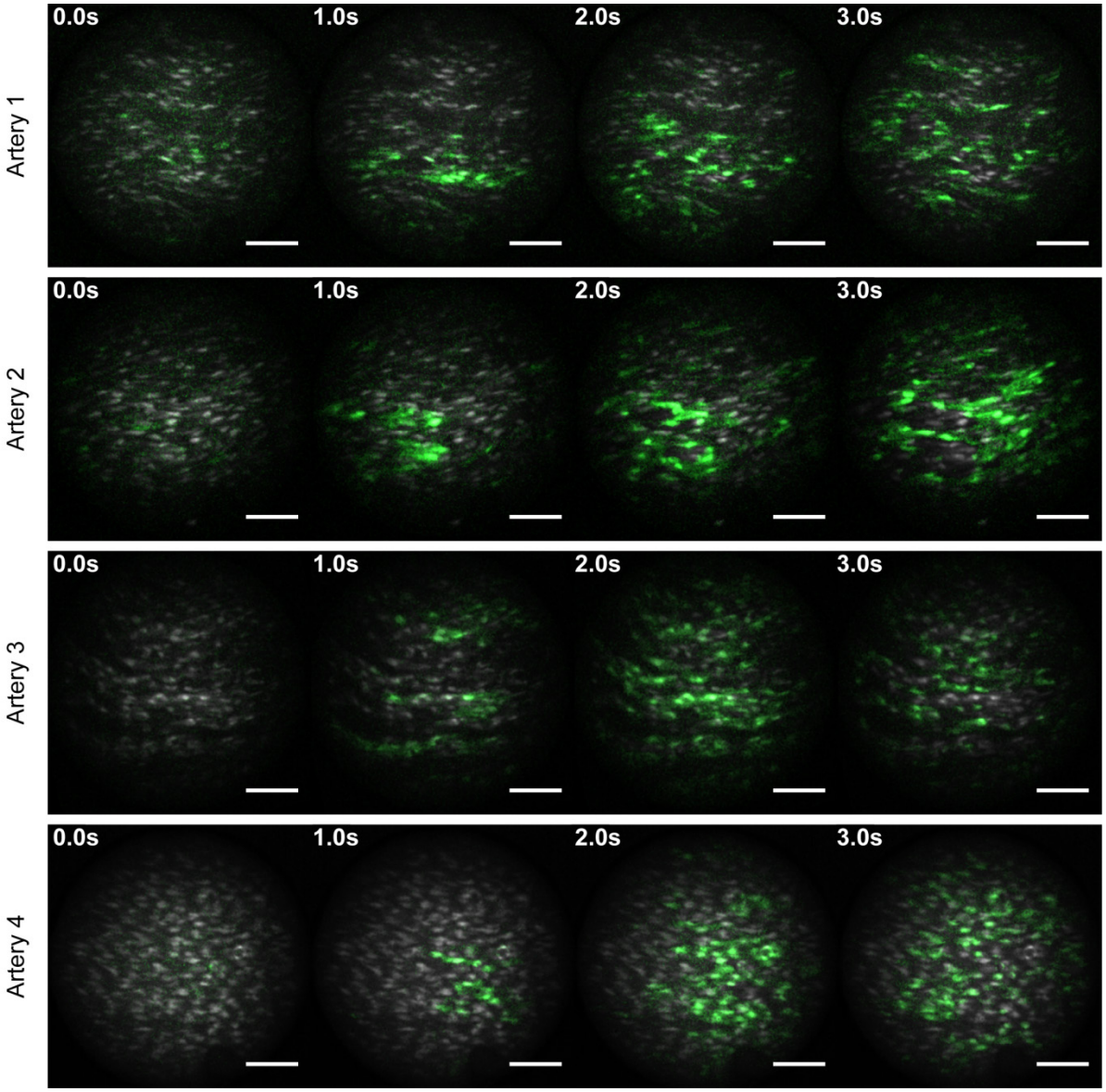

Figure 5. Large-scale, ACh-evoked endothelial Ca^{2+} waves in 4 separate arteries. In each artery, a time-series of Ca^{2+} images from the endothelium illustrates that large-scale, ACh-evoked (100 μM; bath application) Ca^{2+} waves originate in distinct clusters of cells and propagate from there across the endothelium. The images are composed of instantaneous Ca^{2+} activity (green) overlaid on standard deviation images (grayscale), which are indicative of total Ca^{2+} activity. Each bright spot is a single endothelial cell. Scale bars: 100 μm

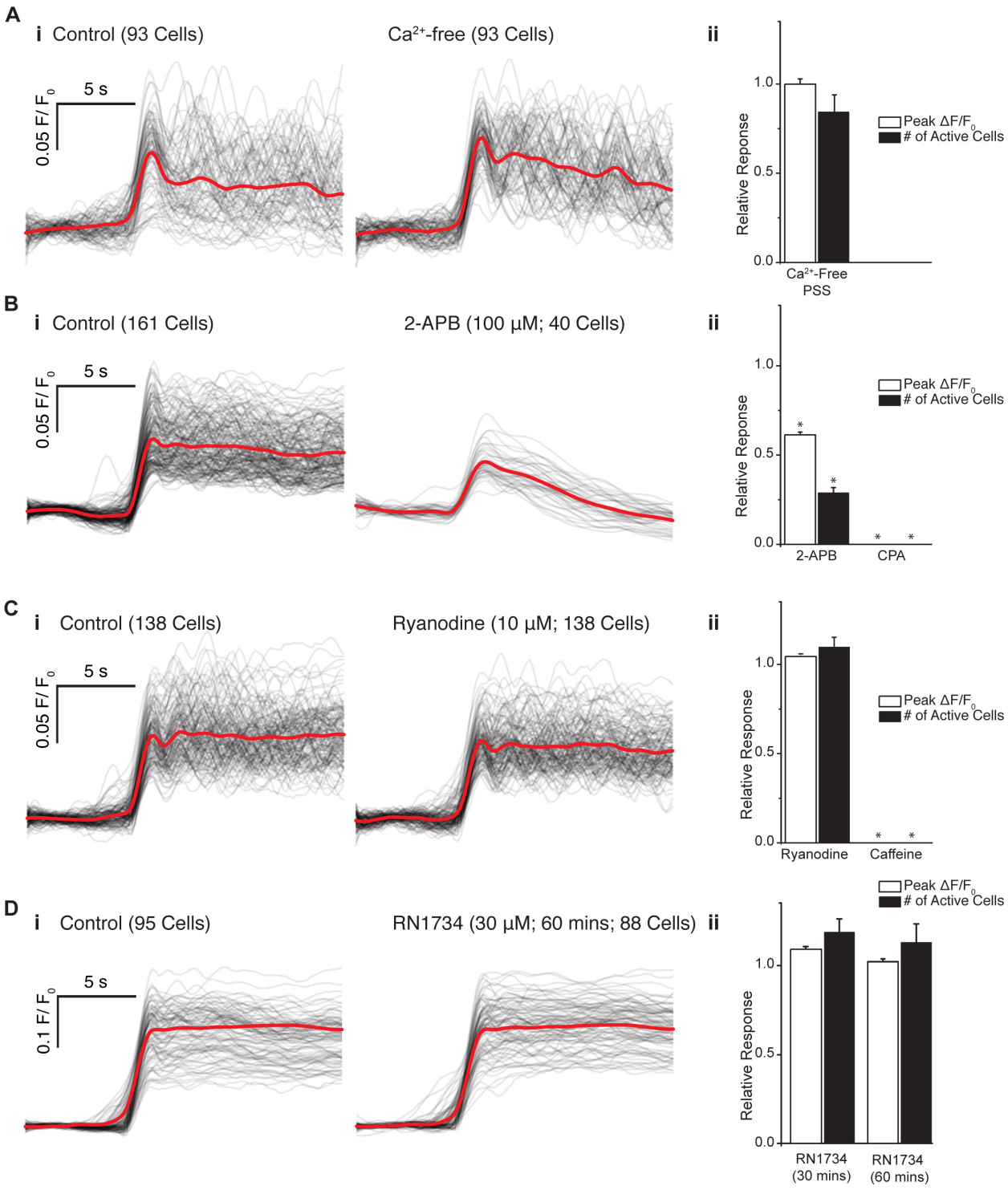

Figure 6. The effects of Ca^{2+}-free bath solution and pharmacological activators and inhibitors on ACh-evoked Ca^{2+} increases. Individual Ca^{2+} traces are shown on the left (i) and summarized data are presented as mean ± SEM and normalized to control (no treatment, 1; not shown) on the right (ii). (Ai & ii) The ACh-evoked Ca^{2+} was comparable before and after the removal of Ca^{2+} from the bath solution (1mM EGTA; n = 4). (Bi & ii) The ACh-evoked Ca^{2+} rise was substantially reduced by aminoethoxydiphenyl borate (2-APB, 100 µM, n = 3) and inhibited by the SERCA blocker cyclopiazonic acid (Bii; CPA, 10 µM, n = 3). (Ci & Cii) ACh-evoked responses persisted in the presence of ryanodine (10 µM; n = 3). Caffeine (10 mM; n = 3; Cii) failed to evoke any Ca^{2+} response. (Di & Dii) ACh-evoked responses were not reduced by the TRPV4 blocker RN1734 (30 µM; n = 3). Individual cellular Ca^{2+} traces are shown in grey with average overlaid in red. $p < 0.05$ was considered significant.

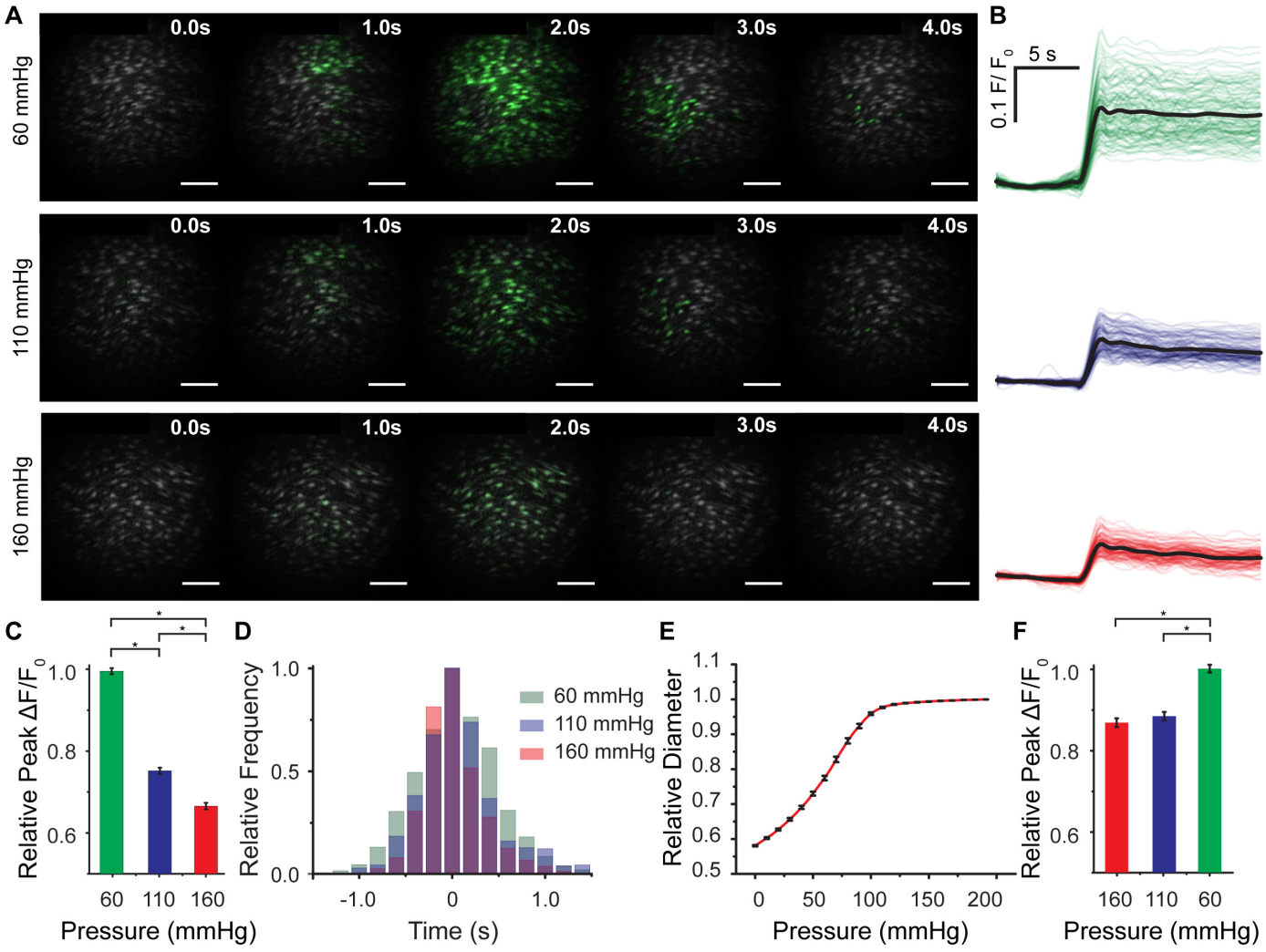

Figure 7. Increased transmural pressure decreases endothelial Ca^{2+} signaling. (A) ACh-evoked Ca^{2+} images from endothelial cells at 60 mmHg (top), 110 mmHg (middle), and 160 mmHg (bottom). Ca^{2+} activity decreased as pressure increased in the three repeated activations of the same artery (20 min wash / re-equilibration period between each ACh application). The data is shown as described in Figure 2A. Scale bar 100 µm. (B) Baseline corrected and aligned Ca^{2+} signals (average overlaid in black and shown in color in the bottom panel) from the Ca^{2+} images shown in (A). (C) Summary data illustrating the pressure-dependent decrease in peak $\Delta F/F_0$ (n = 8, ± SEM). (D) The temporal spread of cellular activation decreases with increased pressure. Note the additional colors in the histogram arises from overlap of colours from the data in 60 mmHg (green), 110 mmHg (blue) and 160 mmHg (red). (E) Summary data illustrating a logistic change in vessel diameter as pressure is increased (from 0 - 200 mmHg; n = 3, ± SEM), measured using the Vessel Diameter plugin for ImageJ. Artery diameter was 1135 ± 110 µm at 60 mmHg, 1429 ± 92 µm at diameter at 110 mmHg and 1460 ± 83 µm at 160 mmHg (n=3). (F) Summary data illustrating an increase in peak $\Delta F/F_0$ as pressure is decreased (n = 6, ± SEM).

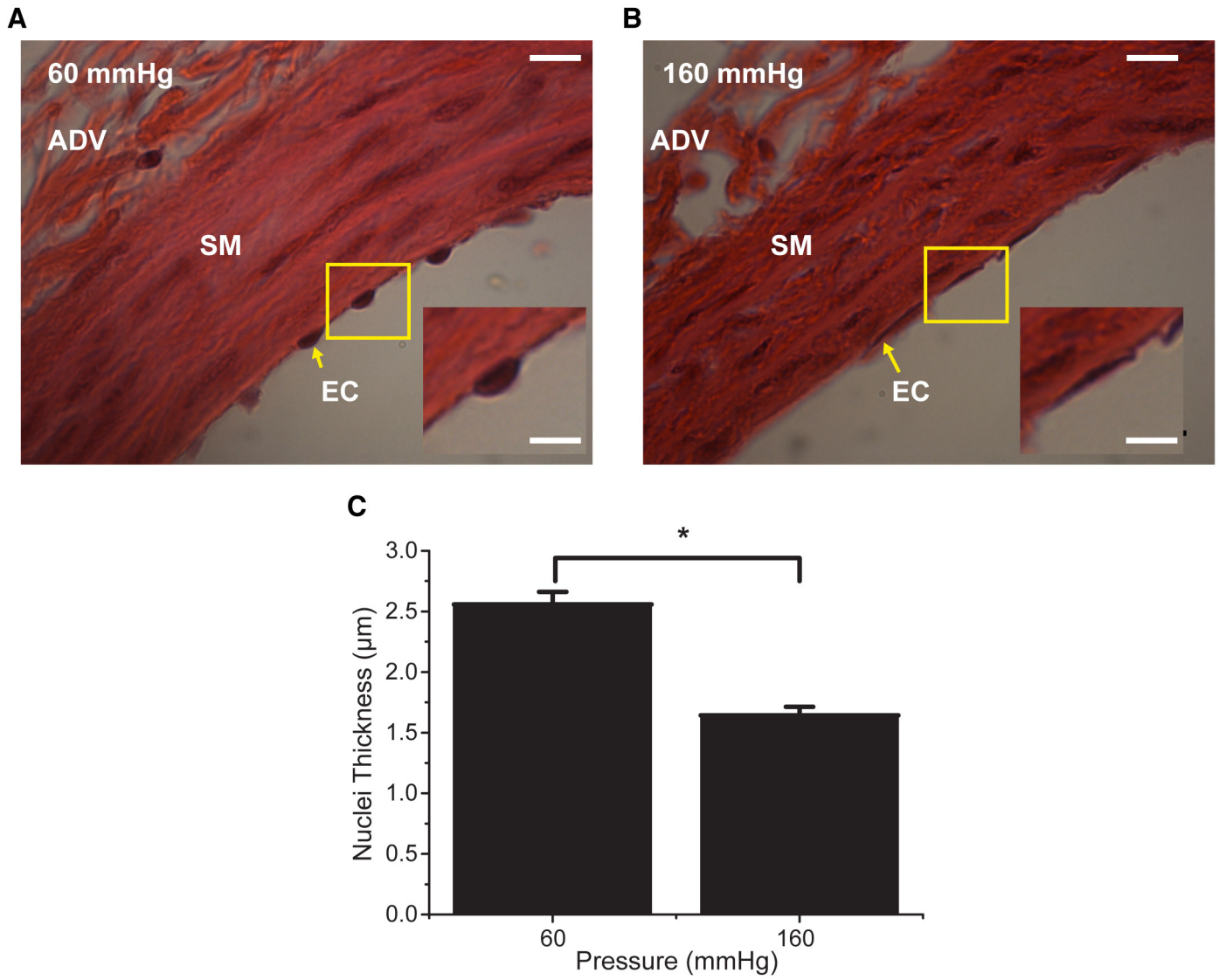

Figure 8. Endothelial cell flattening as intraluminal pressure is increased. Arteries pressurized to 60mmHg (A) and 160 mmHg (B) then fixed show flattening of the endothelial cells (EC) at higher (160 mmHg) pressure. The insets (A,B) shows the yellow box expanded to illustrate the change in shape of single endothelial cells at each pressure. SM - smooth muscle and ADV - adventitia. Scale bars 10 µm main picture, inset 5 µm. (C) Average nuclei thickness (a measure of cell depth) at 60 mmHg and 160 mmHg. At 60 mmHg, n=37 cells from 3 animals; 160 mmHg n=35 cells from 3 animals (*$p<0.05$).

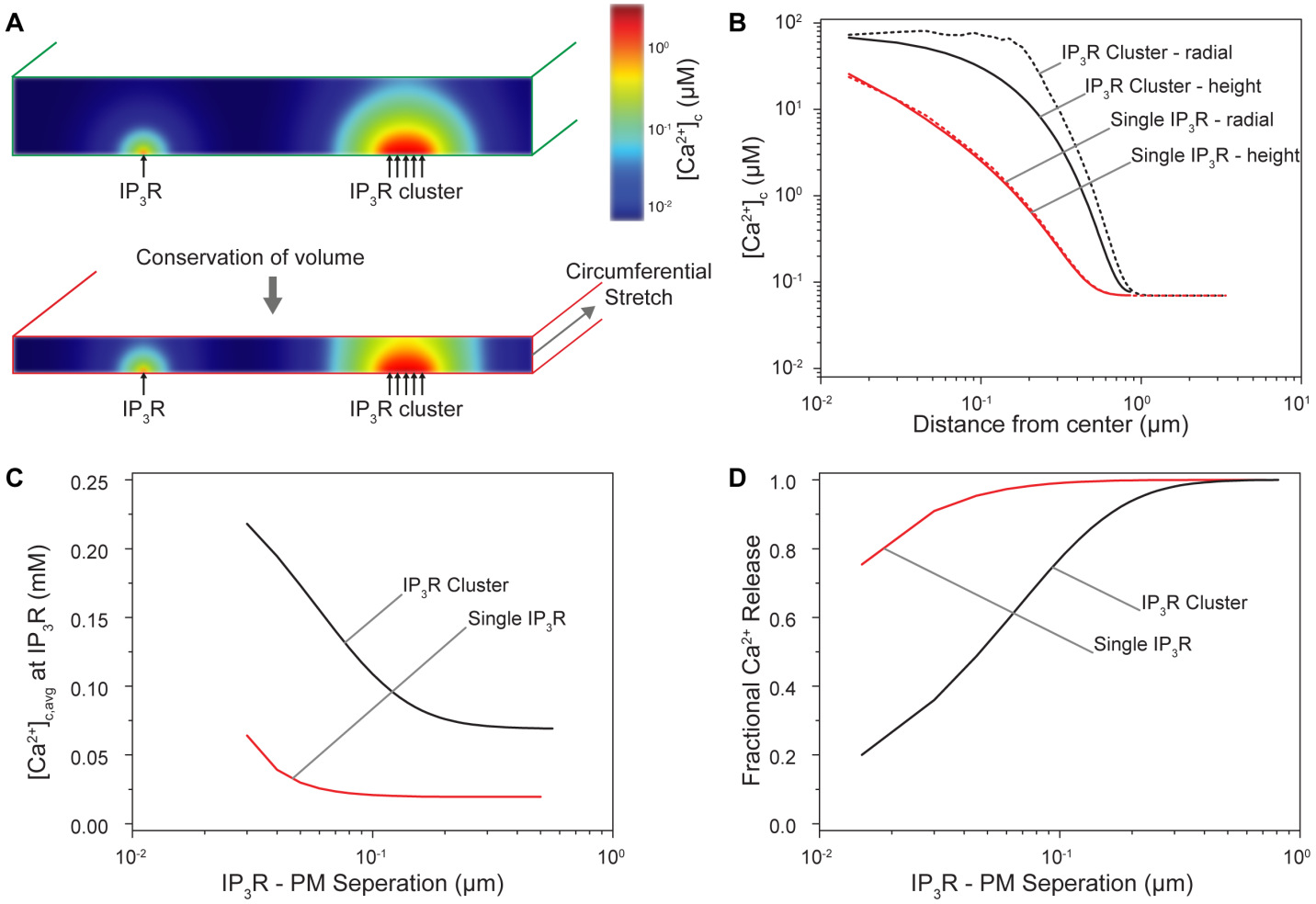

Figure 9. Modelling endoplasmic reticulum Ca^{2+} release from solitary and clusters of IP_3 receptors in cells subject to pressure-induced stretch. (A) Cartoon illustrating the cytosolic Ca^{2+} distribution during Ca^{2+} release through a single IP_3R and a cluster of IP_3Rs as a cell (top, cell height: 0.57 μm) is stretched in the circumferential direction and thins to conserve volume (bottom, cell height: 0.27 μm). (B) Concentration profiles for $[Ca^{2+}]_c$ surrounding individual and clustered IP_3Rs shows that the microdomain of elevated $[Ca^{2+}]_c$ is significantly larger for clusters of receptors (C) The average $[Ca^{2+}]_c$ in the vicinity of IP_3Rs is sensitive to an increasing proximity between the ER and the plasma membrane (cell thinning), resulting in (D), a sensitivity of fractional Ca^{2+} release from internal stores that changes with receptor – plasma membrane distance (cell height) for single IP_3R and a cluster of IP_3Rs, with clusters having sensitivity over significantly larger cell heights, on the order of 500nm.

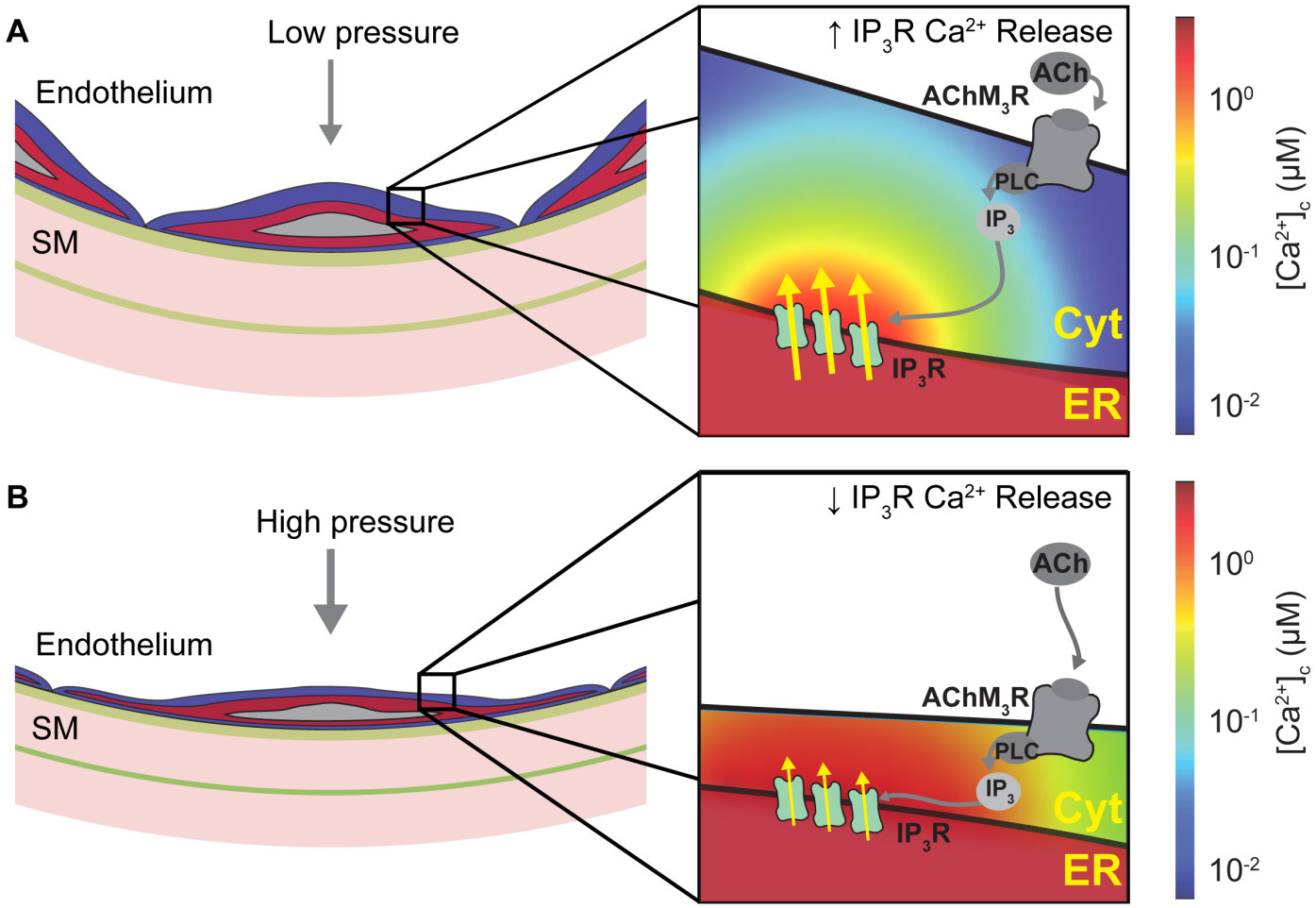

Figure 10. Model of pressure-dependent, geometric suppression of Ca^{2+} release through IP_3Rs. As pressure is increased, from (low, A) (high, B), arterial diameter increases and endothelial cells are stretched along the circumferential. In addition, the radial force of pressure acts upon the cells. To conserve volume, the height of endothelial cells decrease (B). The insets depict the processes leading to changes in ACh-induced Ca^{2+} release in a endothelial cell at low (A, top) and high (B, bottom) pressure. At low pressure activation of IP_3R, after ACh application, results in Ca^{2+} release from the endoplasmic reticulum (ER). Ca^{2+} diffuses rapidly from the release site to maintain a gradient for continued release. The microdomains of Ca^{2+} operates over sizes (300 nm) comparable to the height of an endothelial cell (see text). When pressure is increased (B), the height of the cell decreases and so the distance between the ER and the plasma membrane (PM) also decreases. The decrease in ER-PM distance restricts the diffusion of Ca^{2+} from the release site (IP_3Rs), effectively increasing the local Ca^{2+} microdomain concentration and decreasing the entropic force (indicated by size of yellow arrows) driving Ca^{2+} release through IP_3Rs. The resultant effect is a decrease in Ca^{2+} release from the ER as pressure is increased. SM: smooth muscle.

Grid and Solver			**Reference / notes**
Voxel Scale	dx	0.015 µm	
Solver timestep	dt	0.120 µs	
Courant-Freidcrchs-Lewy condition[Ca^{2+}]	$2Ddtdx^{-2}$ Must be < 1	0.23	Evaluated for Ca^{2+} as most diffusive.
Cytosolic Ca^{2+}			
Equilibrium concentration	C_{inf}	70 nM	(Huang *et al.*, 2000; Means *et al.*, 2006; Bortolozzi *et al.*, 2008)
Diffusion coefficient	$D_{Ca,cyt}$	220 $\mu m^2 s^{-1}$	*(Means et al., 2006)*
Cytosolic buffer - Parvalbumin			
Diffusion coefficient	$D_{B,cyt}$	90 $\mu m^2 s^{-1}$	*(Bortolozzi et al., 2008)*
Diffusion coefficient	$D_{CaB,\ cyt}$	90 $\mu m^2 s^{-1}$	*As for buffer*
Forward binding constant	K_{on}	18.5 $\mu M^{-1} s^{-1}$	*(Bortolozzi et al., 2008)*
Backward binding constant	K_{off}	0.95 s^{-1}	*(Bortolozzi et al., 2008)*
IP_3R			
ER Ca^{2+}concentration	$C_{Ca,er}$	0.25 mM	*(Means et al., 2006)*
Maximum channel current	J_0	$3.3x10^{-19}$ mol s^{-1}	*(Tu et al., 2005; Means et al., 2006)*

Table 1 – Numerical parameters used in reaction diffusion simulations. Rate constants and diffusion coefficients were obtained from (Means *et al.*, 2006; Bortolozzi *et al.*, 2008) and reported as measured in the cytoplasm of cells.

Figure Legends

Figure 1. Endothelial GRIN imaging system (A) Cartoon showing the GRIN microprobe assembly inside a pressurized artery and endothelium (B), A simplified schematic diagram of the GRIN imaging system and the cannulated, pressurized artery. Focusing into the GRIN microprobe with a conventional microscope objective extended the image plane beyond the front surface of the prism and onto the endothelium. The connecting perfusion cannula (B) and pressure servo system permits intraluminal pressure to be controlled and the probe can be refocused if the artery position moves (C). (D) Schematic illustrating the optical emission path through the GRIN microprobe. The GRIN lens recongugates the image plane of a conventional microscope through the length of the cylinder. (E) Schematic illustrating the optical excitation path through the GRIN microprobe. The collimated input excitation light is re-collimated at the output of the GRIN lens. (F) A transmission image of a cannulated artery shows the GRIN microprobe on the right-hand side. (G) 3-dimensional rendering of the custom pressure arteriograph showing the position of the GRIN microprobe assembly and XYZ translation stage for positioning the artery. (H) Picture of setup during live imaging showing the camera and laser arrangement. (I) Fluorescence image of the endothelium visualized using the GRIN imaging system showing some activated cells (see Supplementary Movie S1). Note the field-of-view is circular due to the cross-sectional shape of the GRIN lens. Scale bar 100 μm.

Figure 2. Optical characterization of the side-viewing GRIN imaging system. (A) Normalized intensity profiles, plotted as a function of radius (x) from the center of the circular cross-section of the GRIN lens, of images of fluorescein solution (1 μM) taken with the GRIN microendoscope as the focus was translated along the z-axis. (B) Fluorescence image of 15 μm fluorescent spheres. (C) Raw image of sub-resolution (1.0 μm) fluorescent beads obtained with the microendoscopic imaging system. Vignetting and heterogeneous fluorescence emission from the beads themselves result in apparent variation in size. By rescaling the intensity of the image (insets), beads of apparently different diameter, are shown to be approximately equal in size. (D) Normalized fluorescence intensity profiles, with Gaussian curves fitted, of the two beads highlighted in A. From such intensity profiles, we calculated the optical resolution of our system to be 4.51 ± 0.04 μm (n = 6 beads). Scale bars: 100 μm.

Figure 3. IP_3-evoked Ca^{2+} release simulation (A) Shell density plotted against distance from source (i.e. IP_3R). Theoretical (analytical test case; lines) plots of shell density for a slug of mass released at the origin shows good agreement with our simulated results (circles). (B) Ca^{2+} concentration as a function of radial distance from IP_3Rs. When equilibrated, the Ca^{2+} profile may be approximated by an analytical case (black line), which compares accurately to an examination of our simulation (yellow line). (C) Free Ca^{2+} concentration at an IP_3R as a function of time from receptor opening. The total cytosolic Ca^{2+} rises immediately after IP_3R opening then plateaus as the current flowing through IP_3R and cytosolic Ca^{2+} buffering reaches equilibrium (~0.1ms). See Methods section and Table 1 for equations, source references and parameters used to generate the figures.

Figure 4. Endothelial Ca^{2+} imaging in intact, pressurized (60 mmHg) arteries. (A) Time-series Ca^{2+} images of endothelial cells showing the progression of the Ca^{2+} response evoked by ACh (100 μM; bath applied; 1 μM estimated at the vessel lumen) recorded at 60 mmHg. Images are composed of instantaneous Ca^{2+} activity (green) overlaid on standard deviation images (grayscale) indicative of total Ca^{2+} activity. The rise began in a distinct cluster of cells (see 1 s)

and progressed from there. Each bright spot is an individual cell. Scale bar: 100 μm. (B) ACh-evoked Ca^{2+} signals from the same cells shown in A. In the *left-panel* (unaligned data) the range of times for Ca^{2+} to increase for each of the ~200 cells is approximately 4 seconds. The spread of responses resulted in mean data representing the data poorly. The position of the first peak of derivative signals was used to align Ca^{2+} signals. This procedure synchronizes the Ca^{2+} rises occurring in each due to the action of ACh (*middle panel* 'aligned') and illustrates total Ca^{2+} activity (thick red line) with increased clarity. On successive application of ACh (20 minute reequilibration following wash), the response to ACh was reproducible (right panel). (C) Select examples of unaligned (left) and aligned (right) cellular Ca^{2+} responses from ROIs shown in (A). The gray box illustrates the time point of measurements from aligned signals. (D) Summary data illustrating the reproducibility of Ca^{2+} responses upon repeat application (wash + 20 minute reequilibration) with ACh. Data are presented as mean ± SEM and normalized to control (n = 5; first ACh application, 1; not shown), $p < 0.05$ was considered significant.

Figure 5. Large-scale, ACh-evoked endothelial Ca^{2+} waves in 4 separate arteries. In each artery, a time-series of Ca^{2+} images from the endothelium illustrates that large-scale, ACh-evoked (100 μM; bath application) Ca^{2+} waves originate in distinct clusters of cells and propagate from there across the endothelium. The images are composed of instantaneous Ca^{2+} activity (green) overlaid on standard deviation images (grayscale), which are indicative of total Ca^{2+} activity. Each bright spot is a single endothelial cell. Scale bars: 100 μm.

Figure 6. The effects of Ca^{2+}-free bath solution and pharmacological activators and inhibitors on ACh-evoked Ca^{2+} increases. Individual Ca^{2+} traces are shown on the left (i) and summarized data are presented as mean ± SEM and normalized to control (no treatment, 1; not shown) on the right (ii). (Ai & ii) The ACh-evoked Ca^{2+} was comparable before and after the removal of Ca^{2+} from the bath solution (1mM EGTA; n = 4). (Bi & ii) The ACh-evoked Ca^{2+} rise was substantially reduced by aminoethoxydiphenyl borate (2-APB, 100 μM, n = 3) and inhibited by the SERCA blocker cyclopiazonic acid (Bii; CPA, 10 μM, n = 3). (Ci & Cii) ACh-evoked responses persisted in the presence of ryanodine (10 μM; n = 3). Caffeine (10 mM; n = 3; Cii) failed to evoke any Ca^{2+} response. (Di & Dii) ACh-evoked responses were not reduced by the TRPV4 blocker RN1734 (30 μM; n = 3). Individual cellular Ca^{2+} traces are shown in grey with average overlaid in red. $p < 0.05$ was considered significant

Figure 7. Increased transmural pressure decreases endothelial Ca^{2+} signaling. (A) ACh-evoked Ca^{2+} images from endothelial cells at 60 mmHg (top), 110 mmHg (middle), and 160 mmHg (bottom). Ca^{2+} activity decreased as pressure increased in the three repeated activations of the same artery (20 min wash / re-equilibration period between each ACh application). The data is shown as described in Figure 2A. Scale bar 100 μm. (B) Baseline corrected and aligned Ca^{2+} signals (average overlaid in black and shown in color in the bottom panel) from the Ca^{2+} images shown in (A). (C) Summary data illustrating the pressure-dependent decrease in peak $\Delta F/F_0$ (n = 8, ± SEM). (D) The temporal spread of cellular activation decreases with increased pressure. Note the 4th colour in the histogram (purple) arises from overlap of colours from the data in 110 mmHg (blue) and 160 mmHg (red). (E) Summary data illustrating a logistic change in vessel diameter as pressure is increased (from 0 - 200 mmHg; n = 3, ± SEM), measured using the Vessel Diameter plugin for ImageJ. Artery diameter was 1135 ± 110 μm at 60 mmHg, 1429 ± 92 μm at diameter at 110 mmHg and 1460 ± 83 μm at 160 mmHg (n=3). (F) Summary data illustrating an increase in peak $\Delta F/F_0$ as pressure is decreased (n = 6, ± SEM).

Figure 8. Endothelial cell flattening as intraluminal pressure is increased. Arteries pressurized to 60mmHg (A) and 160 mmHg (B) then fixed show flattening of the endothelial cells (EC) at higher (160 mmHg) pressure. The insets (A,B) shows the yellow box expanded to illustrate the change in shape of single endothelial cells at each pressure. SM - smooth muscle and ADV - adventitia. Scale bars 10 μm main picture, inset 5 μm. (C) Average nuclei thickness (a measure of cell depth) at 60 mmHg and 160 mmHg. At 60 mmHg, n=37 cells from 3 animals; 160 mmHg n=35 cells from 3 animals (*$p<0.05$).

Figure 9. Modelling endoplasmic reticulum Ca^{2+} release from solitary and clusters of IP_3 receptors in cells subject to pressure-induced stretch. (A) Cartoon illustrating the cytosolic Ca^{2+} distribution during Ca^{2+} release through a single IP_3R and a cluster of IP_3Rs as a cell (top, cell height: 0.57 μm) is stretched in the circumferential direction and thins to conserve volume (bottom, cell height: 0.27 μm). (B) Concentration profiles for $[Ca^{2+}]_c$ surrounding individual and clustered IP_3Rs shows that the microdomain of elevated $[Ca^{2+}]_c$ is significantly larger for clusters of receptors (C) The average $[Ca^{2+}]_c$ in the vicinity of IP_3Rs is sensitive to an increasing proximity between the ER and the plasma membrane (cell thinning), resulting in (D), a sensitivity of fractional Ca^{2+} release from internal stores that changes with receptor – plasma membrane distance (cell height) for single IP_3R and a cluster of IP_3Rs, with clusters having sensitivity over significantly larger cell heights, on the order of 500nm.

Figure 10. Model of pressure-dependent, geometric suppression of Ca^{2+} release through IP_3Rs. As pressure is increased, from (low, A) (high, B), arterial diameter increases and endothelial cells are stretched along the circumferential. In addition, the radial force of pressure acts upon the cells. To conserve volume, the height of endothelial cells decrease (B). The insets depict the processes leading to changes in ACh-induced Ca^{2+} release in a endothelial cell at low (A, top) and high (B, bottom) pressure. At low pressure activation of IP_3R, after ACh application, results in Ca^{2+} release from the endoplasmic reticulum (ER). Ca^{2+} diffuses rapidly from the release site to maintain a gradient for continued release. The microdomains of Ca^{2+} operates over sizes (300 nm) comparable to the height of an endothelial cell (see text). When pressure is increased (B), the height of the cell decreases and so the distance between the ER and the plasma membrane (PM) also decreases. The decrease in ER-PM distance restricts the diffusion of Ca^{2+} from the release site (IP_3Rs), effectively increasing the local Ca^{2+} microdomain concentration and decreasing the entropic force (indicated by size of yellow arrows) driving Ca^{2+} release through IP_3Rs. The resultant effect is a decrease in Ca^{2+} release from the ER as pressure is increased. SM: smooth muscle.